Received: 10 March 2020 | Revised: 5 December 2020 | Accepted: 5 December 2020

DOI: 10.1002/nme.6604

Check for updates

RESEARCH ARTICLE

WILEY

# Topology optimization for three-dimensional elastoplastic architected materials using a path-dependent adjoint method

**Diab W. Abueidda**[1,2] | **Ziliang Kang**[3] | **Seid Koric**[1,2] | **Kai A. James**[3] | **Iwona M. Jasiuk**[1,3]

[1]Department of Mechanical Science and Engineering, University of Illinois at Urbana-Champaign, Champaign, Illinois, USA

[2]National Center for Supercomputing Applications, University of Illinois at Urbana-Champaign, Champaign, Illinois, USA

[3]Department of Aerospace Engineering, University of Illinois at Urbana-Champaign, Champaign, Illinois, USA

**Correspondence**
Kai A. James, Department of Aerospace Engineering, University of Illinois at Urbana-Champaign, Champaign, IL, USA.
Email: ijasiuk@illinois.edu (I. M. J.) and Iwona M. Jasiuk, Department of Mechanical Science and Engineering, University of Illinois at Urbana-Champaign, Champaign, IL, USA.
Email: kaijames@illinois.edu (K. A. J.)

**Funding information**
National Science Foundation (NSF) I/UCRC Center, Grant/Award Numbers: IIP-1362146, MOMS-1926353; University of Illinois; University of Illinois at Urbana-Champaign; Zhejiang University; National Science Foundation

**Abstract**

This article introduces a computational design framework for obtaining three-dimensional (3D) periodic elastoplastic architected materials with enhanced performance, subject to uniaxial or shear strain. A nonlinear finite element model accounting for plastic deformation is developed, where a Lagrange multiplier approach is utilized to impose periodicity constraints. The analysis assumes that the material obeys a von Mises plasticity model with linear isotropic hardening. The finite element model is combined with a corresponding path-dependent adjoint sensitivity formulation, which is derived analytically. The optimization problem is parametrized using the solid isotropic material penalization method. Designs are optimized for either end compliance or toughness for a given prescribed displacement. Such a framework results in producing materials with enhanced performance through much better utilization of an elastoplastic material. Several 3D examples are used to demonstrate the effectiveness of the mathematical framework.

**KEYWORDS**

adjoint sensitivity analysis, energy absorption, metamaterials, periodic boundary conditions, von Mises plasticity

## 1 | INTRODUCTION

Recent advances in manufacturing technologies have created many possibilities in materials development.[1] Architected materials are cellular or composite materials possessing combinations of properties unattainable using monolithic materials. Materials with excellent structural properties (stiff, strong, tough, and yet lightweight) are needed for aerospace and automotive industries.[2] Hence, architected materials are of high interest to scientists and engineers. The performance of such architected materials is dependent on the constituent materials, the volume fractions of the constituents, and the architecture (design geometry).[3-9] Nevertheless, most of the approaches used to develop these materials are based on experiments, intuition, and/or bioinspiration.[10,11]

 © 2020 John Wiley & Sons, Ltd. 

Alternatively, topology optimization provides a scientific and systematic framework for generating new designs for structural and material systems with optimized behavior.[12-21] For example, Gao et al.[22] developed an efficient isogeometric topology optimization framework for the design of auxetic metamaterials. The effective properties of periodic architected materials are usually estimated using one unit cell,[1] where the homogenization method and periodic boundary conditions are applied. Thus, it has become popular to combine the topology optimization framework with the homogenization method to obtain material designs that exhibit optimized properties, such as maximum bulk modulus, maximum shear modulus, or negative Poisson's ratio.[14,23-27]

Lately, manufacturing-oriented topology optimization has gained an increasing interest in academia and industry, owing to recent advances in additive manufacturing.[28-30] Most works on architected materials primarily consider the ideal state, where the architected materials are assumed to be defect-free.[7,25,31] Recently, Pasini and Guest[32] discussed the possibility of incorporating imperfections of architected materials in topology optimization frameworks. Zhang et al.[33] introduced a computationally efficient probabilistic method for deterministic structural topology optimization with many load cases; such an approach can be extended to architected materials' design.

While linear elastic topology optimization problems dominate the literature, some researchers have considered material and geometric nonlinearities for structural applications. The sensitivity analyses with incorporated nonlinearities were introduced by Ryu et al.,[13] Tsay and Arora,[34] Vidal et al.,[35] Michaleris et al.,[36] Behrou et al.,[37] Alberdi et al.,[38] and others. Moreover, Swan and Kosaka[39] proposed a framework for optimizing inelastic structures; their analysis included a formulation for viscoelastic and elastoplastic structures. Researchers have also developed optimization frameworks for creating optimized structures exhibiting viscoelastic creep deformation[40] or structures with designs mitigating damage or buckling by enforcing stress, damage, or buckling constraints.[41-44] Others have considered the effect of geometric nonlinearities (finite elasticity) on the optimized structures and materials.[45-50] It is not surprising that these works have inferred that the adoption of nonlinear mechanics greatly impacts the optimized designs providing the loads are large enough to induce nonlinear behavior.

A more customarily investigated material nonlinearity is elastoplasticity.[28,51-55] One of the pioneering studies on elastoplastic topology optimization is the work of Maute et al.[56] The authors maximized the ductility of an elastoplastic structure based on the von Mises yield criterion. Nakshatrala and Tortorelli[57] developed a topology optimization framework for maximizing the energy dissipation under impact loading, where the structural material is assumed to obey von Mises plasticity. Also, Zhang et al.[58] proposed a structural topology optimization framework for anisotropic plastic materials subjected to plane strain conditions. In a different work, a density-based framework for energy-absorbing structures with pressure-dependent yielding is developed.[59] Furthermore, Kato et al.[60] introduced a topology optimization framework for energy dissipation maximization of structural composites wherein they accounted for elastoplastic deformation. Ivarsson et al.[61] proposed and developed a gradient-based topology optimization framework for impact mitigating structures, where the base material undergoes finite strain viscoplastic deformation. Additionally, Ivarsson et al.[62] presented a topology optimization framework for designing viscoplastic microstructures under large deformation, where the periodic boundary conditions are imposed using a master–slave approach on the boundaries of the representative unit cell. Growing attention is also observed for developing topology optimization frameworks for multimaterial structures.[63-66] For instance, Alberdi and Khandelwal[67] proposed a bimaterial topology optimization framework, wherein viscoplastic and hyperelastic phases are combined to maximize energy dissipation.

The lack of unit cell upscaling methods, precisely homogenization method based on asymptotic expansion, when nonlinear mechanics are involved, forms a challenge for the evaluation of the effective properties, which in turn makes the topology optimization of materially nonlinear systems more difficult than in the case of linear elasticity.[1,32] A few papers in the literature have considered topology optimization frameworks for effective material properties that dictate the incorporation of material and geometric nonlinearities.[1,68-72] For instance, the challenges with upscaling methods accompanying nonlinear properties encouraged Carstensen et al.[73] to use structures with finite periodicity to calculate optimized energy absorption. Although the elastoplastic topology optimization literature has a few attempts tackling the creation of architected materials with maximum energy absorption,[72] it still lacks frameworks considering other design objectives. Examples of other objective functions that are useful for various engineering applications are strength[2,74-76] and end compliance,[77-79] where such objectives have not been thoroughly studied within the scope of elastoplastic materials, especially for three-dimensional (3D) architected materials.

In this article, we develop a topology optimization framework for two different objective functions (engineering toughness and end compliance). The outputs of the framework are 3D architected cellular materials made from an

elastoplastic base material with linear isotropic hardening and von Mises yield criterion. The finite element (FE) analysis and topology optimization framework are based on a 3D working domain, where periodic boundary conditions have been imposed on a representative unit cell (RUC). The average stress is computed using the finite element reaction forces to optimize the desired properties, where the unit cell is subject to uniaxial or shear strain, and the periodicity is enforced using Lagrange multipliers. Also, attention is paid to study the effect of the initial design and to impose microstructural connectivity through enforcing proper constraints. The sensitivities are obtained using a path-dependent adjoint method.

Thus, there are several novel aspects of this article. We account for periodicity using the Lagrange multiplier method. Another essential difference between this approach and the other work available in the literature is that we compute the average stress using the nodal reactions to define the objective functions. Hence, the derivation of the adjoint sensitivities is different. Additionally, we have derived the adjoint sensitivities for two objective functions, and we compare the responses obtained from the different objective functions. Finally, we consider 3D elastoplastic metamaterials.

The remainder of the article is laid out as follows: Section 2 provides an overview of the general topology optimization problem. Section 3 discusses the nonlinear finite element analysis (FEA) and the elastoplasticity model adopted. Section 4 talks about the discretization and parametrization using the solid isotropic material penalization (SIMP) method.[80,81] Also, Section 4 states the objective functions and scrutinizes the derivation of the equations used in the sensitivity analysis. In Section 5, we present several 3D numerical examples along with analysis and discussion of the results. We conclude the article in Section 6 by summarizing the significant results and stating possible directions for future work.

## 2 | PROBLEM OVERVIEW

In the present article, the topology optimization problem is addressed as a material distribution problem. The first step is to define a working domain that is the physical region in which the material is distributed to obtain an optimized response. Figure 1 demonstrates the generalized material distribution problem, where $\Lambda$ denotes the working domain, and $\Omega$ embodies the material domain. Mathematically, $\Lambda$ is a bounded set in 3D space $\mathbb{R}^3$ containing all admissible designs $\Omega$. The material boundary $\Gamma$ represents the surfaces on which prescribed displacements and tractions are applied, respectively.

In topology optimization, the objective function $G$ is maximized to identify an optimized material distribution $\Omega^*$. The objective function depends on the displacement field $\mathbf{u}$ and how the material ($\Omega$) is distributed within $\Lambda$. Mathematically, the optimization problem can be written as follows

$$\begin{aligned} &\max_{\Omega \subset \Lambda} G(\Omega) \\ &\textit{subject to} : h_i(\Omega) \leq 0, \quad i = 1, 2, \dots, n_i \\ &\qquad \widetilde{h}_j(\Omega) = 0, \quad j = 1, 2, \dots, n_e, \end{aligned} \tag{1}$$

where $\{h_i\}$ and $\{\widetilde{h}_j\}$ represent the sets of inequality and equality constraints, respectively. Also, $n_i$ and $n_e$ denote the number of inequality and equality constraints, respectively.

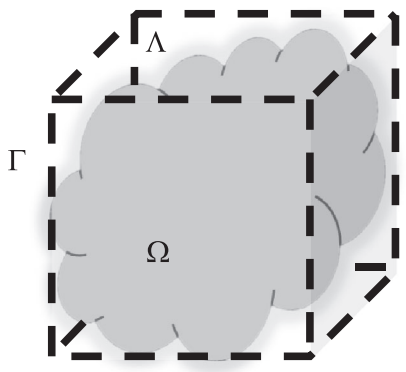


**FIGURE 1** The material distribution problem with prescribed displacement and traction boundary conditions

The governing equations describing the mechanics of structures or materials guide the optimization search. The equilibrium equation in the absence of inertial and body forces is given by

$$\nabla \cdot \boldsymbol{\sigma} = \mathbf{0} \; in \; \Omega, \tag{2}$$

where $\boldsymbol{\sigma}$ is the Cauchy stress tensor, while $\boldsymbol{\nabla} \cdot$ is the divergence operator. Under the assumption of small deformations, the kinematic equation is expressed as

$$\boldsymbol{\varepsilon} = \frac{1}{2}\left(\nabla \mathbf{u} + (\nabla \mathbf{u})^T\right), \tag{3}$$

where $\boldsymbol{\varepsilon}$ is the infinitesimal strain tensor, $\boldsymbol{\nabla}$ is the gradient operator, and $(\bullet)^T$ is the transpose operator. Periodic boundary conditions are imposed on the RUC for better representation of periodic medium.[72,82-84] The boundary $\Gamma$ is divided into opposing regions $\Gamma^+$ and $\Gamma^-$ such that $\Gamma^+ \cap \Gamma^-$ and $\Gamma = \Gamma^+ + \Gamma^-$, where $\boldsymbol{x}^+ \in \Gamma^+$ and $\boldsymbol{x}^- \in \Gamma^-$. The periodicity constraints imposed on the RUC can be expressed as:

$$\mathbf{u}(\boldsymbol{x}^+) - \mathbf{u}(\boldsymbol{x}^-) = \bar{\boldsymbol{\varepsilon}} \cdot \boldsymbol{l} \; on \; \Gamma, \tag{4}$$

where $\bar{\boldsymbol{\varepsilon}}$ is the macroscopic strain tensor driving the deformation in the boundary value problem (BVP), and $\boldsymbol{l} = \boldsymbol{x}^+ - \boldsymbol{x}^-$.

## 3 | ELASTOPLASTIC FINITE ELEMENT ANALYSIS

In this section, we briefly mention the main finite element equations.[85,86] Consider a solid body exhibiting an elastoplastic response and occupying the material domain $\Omega$, as depicted in Figure 1. At each material point in $\Omega$, the stress tensor $\boldsymbol{\sigma}$ is defined by the material constitutive model discussed later. The weak form of the BVP in the absence of inertial and body forces is expressed as

$$\int_{\Omega} \boldsymbol{\sigma} \, : \, \nabla \delta \mathbf{u} dv - \int_{\Gamma} \mathbf{t} \cdot \delta \mathbf{u} ds = 0, \tag{5}$$

where $\delta \mathbf{u}$ is the arbitrary virtual displacement, and $\mathbf{t}$ denotes the traction. The global residual vector $\mathbf{R}_1$ is given by

$$\mathbf{R}_1(\mathbf{u}) = \mathbf{F}_{int} - \mathbf{P}. \tag{6}$$

where $\mathbf{F}_{int}$ is the internal force vector, and $\mathbf{P}$ is the external force vector. The global force vectors (in the absence of body forces) are given by

$$\begin{aligned} \mathbf{F}_{int} &= \mathop{\mathscr{A}}_{e=1}^{N_{ele}} \mathbf{F}^e_{int} \text{ where } \mathbf{F}^e_{int} = \int_{\Omega^e} \mathbf{B}^T \boldsymbol{\sigma} dv, \\ \mathbf{P} &= \mathop{\mathscr{A}}_{e=1}^{N_{ele}} \mathbf{P}^e \text{ where } \mathbf{P}^e = \int_{\Gamma^e} \mathbf{N}^T \mathbf{t} ds, \end{aligned} \tag{7}$$

where $\mathscr{A}$ is the FE assembly operator, the superscript $e$ denotes the element, $N_{ele}$ denotes the total number of elements, $\mathbf{N}$ denotes the shape function matrix, and $\mathbf{B}$ represents the shape function derivative matrix.

In the present article, we implement a displacement-control method, where the periodic boundary conditions are directly applied to the degrees of freedom on the discretized $\Gamma$, that is, they are imposed in a pointwise fashion. The discrete form of the periodic constraints, shown in Equation (4), is written as

$$\mathbf{A}\mathbf{u} - \boldsymbol{l}\hat{\bar{\boldsymbol{\varepsilon}}} = \mathbf{0}, \tag{8}$$

where for the 3D case, $\hat{\bar{\boldsymbol{\varepsilon}}} = \left[\bar{\varepsilon}_{11} \;\; \bar{\varepsilon}_{22} \;\; \bar{\varepsilon}_{33} \;\; 2\bar{\varepsilon}_{12} \;\; 2\bar{\varepsilon}_{23} \;\; 2\bar{\varepsilon}_{31}\right]^T$. The matrix $\boldsymbol{l}$ contains the information about the length of the unit cell. In this article, we consider cubic unit cells, that is, $l_1 = l_2 = l_3 = l$. The matrix $\mathbf{A}$ relates

degrees of freedom on the opposing regions $\Gamma^+$ and $\Gamma^-$. For an arbitrary pair $j$ of boundary nodes, Equation (8) is expressed as:

$$\mathbf{A}^j\mathbf{u}^j - \boldsymbol{l}^j\hat{\bar{\boldsymbol{\varepsilon}}} = \begin{bmatrix} 1 & 0 & 0 & -1 & 0 & 0 \\ 0 & 1 & 0 & 0 & -1 & 0 \\ 0 & 0 & 1 & 0 & 0 & -1 \end{bmatrix} \begin{bmatrix} u_j^+ \\ v_j^+ \\ w_j^+ \\ u_j^- \\ v_j^- \\ w_j^- \end{bmatrix} - \begin{bmatrix} l & 0 & 0 & l/2 & 0 & l/2 \\ 0 & l & 0 & l/2 & l/2 & 0 \\ 0 & 0 & l & 0 & l/2 & l/2 \end{bmatrix} \begin{bmatrix} \bar{\varepsilon}_{11} \\ \bar{\varepsilon}_{22} \\ \bar{\varepsilon}_{33} \\ 2\bar{\varepsilon}_{12} \\ 2\bar{\varepsilon}_{23} \\ 2\bar{\varepsilon}_{13} \end{bmatrix} = \begin{bmatrix} 0 \\ 0 \\ 0 \end{bmatrix}. \tag{9}$$

The periodicity constraints are enforced using Lagrange multipliers $\boldsymbol{\theta}$. The residuals $\mathbf{R}$ are expressed as

$$\mathbf{R}(\mathbf{u}, \boldsymbol{\theta}) = \begin{bmatrix} \mathbf{R}_1(\mathbf{u}, \boldsymbol{\theta}) \\ \mathbf{R}_2(\mathbf{u}) \end{bmatrix} = \begin{bmatrix} \mathbf{F}_{int}(\mathbf{u}) - \mathbf{A}^T\boldsymbol{\theta} \\ \mathbf{A}\mathbf{u} - \boldsymbol{l}\hat{\bar{\boldsymbol{\varepsilon}}} \end{bmatrix} = \begin{bmatrix} \mathbf{0} \\ \mathbf{0} \end{bmatrix}. \tag{10}$$

Equation (10) is solved using the Newton–Raphson method utilizing the Jacobian matrix $\mathbf{J}$

$$\begin{aligned} \mathbf{K} &= \mathop{\mathscr{A}}_{e=1}^{N_{ele}} {}^e\mathbf{k} \ with \ {}^e\mathbf{k} = \int_{\Omega^e} \mathbf{B}^T\mathbf{C}_T\mathbf{B}dv, \\ \mathbf{J} &= \begin{bmatrix} \partial\mathbf{R}_1/\partial\mathbf{u} & \partial\mathbf{R}_1/\partial\boldsymbol{\theta} \\ \partial\mathbf{R}_2/\partial\mathbf{u} & \partial\mathbf{R}_2/\partial\boldsymbol{\theta} \end{bmatrix} = \begin{bmatrix} \mathbf{K} & -\mathbf{A}^T \\ \mathbf{A} & \mathbf{0} \end{bmatrix}, \\ \mathbf{J} &\begin{bmatrix} d\mathbf{u} \\ d\boldsymbol{\theta} \end{bmatrix} + \begin{bmatrix} \mathbf{0} \\ -\boldsymbol{l} \end{bmatrix} \hat{\bar{\boldsymbol{\varepsilon}}} = \begin{bmatrix} \mathbf{0} \\ \mathbf{0} \end{bmatrix}, \end{aligned} \tag{11}$$

where $\mathbf{K}$ is the tangent stiffness matrix, ${}^e\mathbf{k}$ is the element stiffness matrix, and $\mathbf{C}_T$ is the algorithmic consistent tangent modulus coming from the linearization of the constitutive model adopted.

Next, we provide a short description of the constitutive relations (elastoplasticity) and radial return mapping,[87] used to ensure that the yield condition is satisfied at each load increment. The small strain plasticity theory allows us to decompose the total strain tensor $\boldsymbol{\varepsilon}$ additively

$$\boldsymbol{\varepsilon} = \boldsymbol{\varepsilon}^{el} + \boldsymbol{\varepsilon}^{p}, \tag{12}$$

where the superscripts $el$ and $p$ denote the elastic and plastic parts of the strain tensor, respectively. The Cauchy stress tensor $\boldsymbol{\sigma}$ is defined by

$$\boldsymbol{\sigma} = \mathbb{C}^{el} : \boldsymbol{\varepsilon}^{el}, \ \mathbb{C}^{el} := \kappa\mathbf{1} \otimes \mathbf{1} + 2\mu\left(\mathbf{I} - \frac{1}{3}\mathbf{1} \otimes \mathbf{1}\right), \tag{13}$$

where $\mathbb{C}^{el}$ is the isotropic elasticity tensor, $\kappa$ is the bulk modulus, $\mu$ is the shear modulus, $\mathbf{1}$ is the second-order identity tensor, and $\mathbf{I}$ is a fourth-order tensor whose components are defined as $\mathrm{I}_{ijkl} = \frac{1}{2}(\delta_{ik}\delta_{jl} + \delta_{jk}\delta_{il})$ where $\delta$ is the Kronecker delta. Here, we use the von Mises yield condition $\psi$, which is widely used to describe metal plasticity.

$$\psi(\boldsymbol{\sigma}, \alpha) = \|\mathbf{s}\| - \sqrt{2/3}(\sigma_y + K\alpha) = 0, \tag{14}$$

where $\alpha$ is the internal plastic variable known as equivalent plastic strain, $K$ denotes the linear isotropic hardening modulus, $\sigma_y$ is the initial yield stress, and $\mathbf{s}$ denotes the deviatoric stress.

The evolutions of the plastic strain $\dot{\boldsymbol{\varepsilon}}^p$ and equivalent plastic strain $\dot{\alpha}$ are defined by the associative flow rules

$$\dot{\boldsymbol{\varepsilon}}^p = \gamma \frac{\partial \psi}{\partial \boldsymbol{\sigma}} = \gamma \mathbf{n}, \;\; \mathbf{n} \coloneqq \frac{\mathbf{s}}{\|\mathbf{s}\|}, \;\; \dot{\alpha} = \gamma \frac{\partial \psi}{\partial \boldsymbol{\sigma}} = \sqrt{\frac{2}{3}}\gamma, \tag{15}$$

where $\gamma$ is the consistency parameter, and $\mathbf{n}$ denotes the normal to the yield surface. The Karush–Kuhn–Tucker (KKT) conditions and consistency condition are needed to complete the definition of the constitutive model

$$\psi(\boldsymbol{\sigma}, \alpha) \leq 0, \;\; \gamma \psi(\boldsymbol{\sigma}, \alpha) = 0, \;\; \gamma \geq 0, \tag{16}$$

$$\gamma \dot{\psi}(\boldsymbol{\sigma}, \alpha) = 0, \tag{17}$$

where Equation (16) summarizes the KKT conditions, and Equation (17) represents the consistency condition. To avoid any confusion, note that the KKT conditions defined in Equation (16) are different from the KKT conditions used for the convergence criteria for the numerical optimization problem.

The radial return mapping algorithm, originally proposed by Wilkins,[88] is adopted here. Given the state at an integration point: $\boldsymbol{\varepsilon}_{n+1}$ at the current time step $n+1$, and $\boldsymbol{\varepsilon}^p_n$ and $\alpha_n$ at the previous step $n$, one can find $\boldsymbol{\varepsilon}^p_{n+1}$, $\alpha_{n+1}$, and $\mathbf{C}_{T_{n+1}}$.[87] We start with computing an elastic trial stress tensor $\mathbf{s}^{trial}$

$$\begin{aligned} \mathbf{e}_{n+1} &= \boldsymbol{\varepsilon}_{n+1} - \frac{1}{3}\left(trace[\boldsymbol{\varepsilon}_{n+1}]\right)\mathbf{1} \\ \mathbf{s}^{trial}_{n+1} &= 2\mu\left(\mathbf{e}_{n+1} - \mathbf{e}^p_n\right) \end{aligned} \tag{18}$$

where $\mathbf{e}$ is the deviatoric strain tensor. Then, we check the yield condition

$$\psi^{trial}_{n+1} = \|\mathbf{s}^{trial}_{n+1}\| - \sqrt{2/3}(\sigma_y + K\alpha). \tag{19}$$

If $\psi^{trial}_{n+1} \leq 0$, we set $(\bullet)_{n+1} = (\bullet)^{trial}_{n+1}$ and $\mathbf{C}_T = \mathbb{C}^{el}$. Otherwise, we proceed with the computations of $\mathbf{n}_{n+1}$, $\alpha_{n+1}$, and $\Delta\gamma_{n+1}$

$$\mathbf{n}_{n+1} = \frac{\mathbf{s}^{trial}_{n+1}}{\|\mathbf{s}^{trial}_{n+1}\|}, \;\; \Delta\gamma_{n+1} = \frac{\psi^{trial}_{n+1}}{2\left(\mu + \frac{K}{3}\right)}, \;\; \alpha_{n+1} = \alpha_n + \sqrt{2/3}\,\Delta\gamma_{n+1}. \tag{20}$$

Next, we update the plastic strain and stress

$$\begin{aligned} \mathbf{e}^p_{n+1} &= \mathbf{e}^p_n + \Delta\gamma_{n+1}\,\mathbf{n}_{n+1} \\ \boldsymbol{\sigma}_{n+1} &= \kappa\; trace[\boldsymbol{\varepsilon}_{n+1}]\mathbf{1} + \mathbf{s}^{trial}_{n+1} - 2\mu\,\Delta\gamma_{n+1}\,\mathbf{n}_{n+1}. \end{aligned} \tag{21}$$

The consistent tangent modulus is obtained using

$$\begin{aligned} \mathbf{C}_T &= \kappa \mathbf{1} \otimes \mathbf{1} + 2\mu\,\chi_{n+1}\left(\mathbf{I} - \frac{1}{3}\mathbf{1} \otimes \mathbf{1}\right) - 2\mu\,\overline{\chi}_{n+1}\,\mathbf{n}_{n+1} \otimes \mathbf{n}_{n+1} \\ \chi_{n+1} &\coloneqq 1 - \frac{2\mu\Delta\gamma_{n+1}}{\|\mathbf{s}^{trial}_{n+1}\|}, \;\; \overline{\chi}_{n+1} \coloneqq \frac{1}{1 + \frac{K}{3\mu}} - (1 - \chi_{n+1}). \end{aligned} \tag{22}$$

## 4 | OPTIMIZATION FRAMEWORK

### 4.1 | Design parametrization

The optimization problem can be solved by identifying elements that should be contained within the material region, or it can be solved by directly optimizing the location of the material boundary $\Gamma$.[12,89,90] Here, we adopt the former approach

and use the SIMP method.[80,81] Based on this approach, the finite elements in the working domain $\Lambda$ are interpolated via a material density vector $\boldsymbol{\phi}$ with components $\phi \in [0, 1]$, where $\phi = 0$ indicates a void element, and $\phi = 1$ corresponds to a solid element. Penalty factors are introduced to steer the solution to a binary (0, 1) design and avoid elements with intermediate densities. Three penalty factors $(p_1, p_2, p_3)$ are required to interpolate three material parameters for an element $e$, namely Young's modulus $E_e$, initial yield stress $\sigma_{y_e}$, and hardening modulus $K_e$, respectively.

$$\begin{aligned} E_e &= E_{min} + (E - E_{min})\phi_e^{p_1}, \\ \sigma_{y_e} &= \sigma_{y_{min}} + (\sigma_y - \sigma_{y_{min}})\phi_e^{p_2}, \\ K_e &= K_{min} + (K - K_{min})\phi_e^{p_3}, \end{aligned} \tag{23}$$

where $E$, $\sigma_y$, and $K$ denote the material parameters for a solid element ($\phi = 1$). On the other hand, $E_{min} = 10^{-6}E$, $\sigma_{y_{min}} = 10^{-6}\sigma_y$, and $K_{min} = 10^{-6}K$ are the material parameters for a void element ($\phi \approx 0$), and they are assigned values slightly higher than zero to avoid singularity of the stiffness matrix. A continuation scheme is used to gradually increase the penalization factors.

The element-based formulation, in combination with first-order elements, suffers from numerical instabilities such as checkerboarding and mesh-dependence.[91,92] The density filtering technique, introduced by Bruns et al.,[49] is utilized to address such numerical instabilities. Following this approach, the pseudo-densities $\boldsymbol{\xi}$, which are the design variables directly manipulated by the optimizer, are related to the physical (filtered) densities $\boldsymbol{\phi}$, used to construct the global stiffness matrix via Equation (23):

$$\begin{aligned} \boldsymbol{\phi} &= \overline{\boldsymbol{W}}\boldsymbol{\xi} \\ q_{ij} &= \max(0, r_{min} - \|\boldsymbol{X}_i - \boldsymbol{X}_j\|) \\ \overline{q}_{ij} &= \frac{1}{\sum_{k=1}^{N_{r_{\min}}} q_k} q_{ij} \end{aligned} \tag{24}$$

where $q_{ij}$ is the weighting coefficient, $\overline{q}_{ij}$ is the normalized weight coefficient composing the normalized filter matrix $\overline{\boldsymbol{W}}$, $\boldsymbol{X}$ are the coordinates of the element centroid, and $r_{min}$ is the filter radius. Since the mesh of the working domain is fixed throughout the optimization, the normalized filter matrix $\overline{\boldsymbol{W}}$ is calculated once at the beginning of the optimization problem and then stored to be used during each optimization iteration.

## 4.2 | Objective functions

To quantify the effective properties of materials, usually one applies a known average strain with periodic boundary conditions, and then the average stress is calculated using the mean stress theorem:

$$\overline{\sigma}_{ij} = \frac{1}{V}\int_{\Omega} \sigma_{ij} dV. \tag{25}$$

Also, the average stress can be evaluated from the nodal reactions by employing the divergence theorem.[82,83,93] The primary objective of the present article is to develop a framework to maximize either toughness or end compliance of cellular materials for a given prescribed displacement (or applied average strain). The above two objective functions are maximized under two scenarios: uniaxial ($\overline{\varepsilon}_{11} \neq 0$ and other components are zero) and pure shear ($\overline{\varepsilon}_{12} \neq 0$ and other components are zero) strains. Figure 2 portrays the strains for these two different scenarios. We start by stating the objective functions. The first objective function considered here is the end compliance. When the end compliance is maximized for a given prescribed displacement, the magnitude of the load that corresponds to the given prescribed displacement is maximized. Assuming the analysis is solved in $M$ increments, the end compliance is mathematically expressed as:

$$G_{end\ compliance} = \mathbf{P}_M^T \cdot \mathbf{u}_M. \tag{26}$$

Note that the problem is displacement-controlled, and it has no external forces directly applied to the RUC. Thus, the external force vector $\mathbf{P}$ is composed of reaction forces due to the prescribed displacement and periodicity constraints, and it is zero for the remaining degrees of freedom.

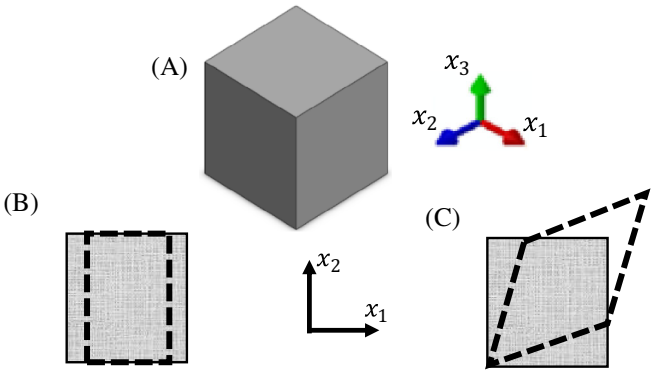


**FIGURE 2** (A) Illustration of the working domain. Demonstration of the strains considered in this study: (B) uniaxial compression and (C) pure shear. Note that (B) and (C) are in the $x_1x_2$-plane

The second considered objective function is toughness, defined here as the energy absorbed by the material at a predetermined strain. The toughness is estimated using the rectangular rule, a simple numerical integration technique, as follows:

$$Toughness \approx \sum_{n=1}^{M} F_n \, \Delta d_n, \tag{27}$$

where $d$ represents the prescribed displacement at step $n$, and $M$ is the total number of increments. Since the prescribed displacement is incrementally applied with a constant displacement increment, the displacement increment $\Delta d_n$ is dropped from the definition of the objective function $G$ and its gradients, that is,

$$G_{toughness} = \sum_{n=1}^{M} F_n, \tag{28}$$

where $F$ at step $n$ is written as:

$$F_n = \boldsymbol{L}^T \mathbf{P}_n, \tag{29}$$

where $\boldsymbol{L}$ is a vector defined to specify the degrees of freedom used in the computation of $F_n$. In the case of uniaxial strain (see Figure 2(B)), $L_i$ is expressed as:

$$L_i = \begin{cases} -1 & i \in x_1^+ \text{ and in } x_1\text{-direction} \\ +1 & i \in x_1^- \text{ and in } x_1\text{-direction}, \\ 0 & \text{otherwise} \end{cases} \tag{30}$$

where $i$ is the degree of freedom. In the case of pure shear (see Figure 2(C)), $L_i$ is defined as:

$$L_i = \begin{cases} +1 & i \in x_1^+ \text{ and in } x_2\text{-direction or } i \in x_2^+ \text{ and in } x_1\text{-direction} \\ -1 & i \in x_1^- \text{ and in } x_2\text{-direction or } i \in x_2^- \text{ and in } x_1\text{-direction} \\ 0 & \text{otherwise} \end{cases}. \tag{31}$$

## 4.3 | Problem formulation

Here, we seek optimized topologies yielding cellular materials possessing enhanced performance, given a certain mass constraint. Also, an elastic compliance constraint is enforced to maintain the integrity of the design and ensure some requisite stiffness with respect to the applied load. Since the problem is a displacement-controlled one, a lower bound on the minimum allowable compliance is imposed. However, in the case of a force-controlled problem, stiffness constraints are enforced by placing an upper bound on the maximum allowable compliance. Note that the elastic compliance constraints are computed for three axial strain cases, different from the applied loading used to calculate the objective function.

Also, note that the three axial strains used for the constraints are small enough not to induce any plastic deformation. Mathematically, the optimization problem is expressed as:

$$\begin{aligned} &\max_{\Omega \subset \Delta} G \\ \text{subject to}: \; & h_1 = C_{min} - \mathbf{P}_{x_1}^T \mathbf{u} \leq 0 \\ & h_2 = C_{min} - \mathbf{P}_{x_2}^T \mathbf{u} \leq 0 \\ & h_3 = C_{min} - \mathbf{P}_{x_3}^T \mathbf{u} \leq 0 \\ & h_4 = V(\boldsymbol{\xi}) - V_f \leq 0, \end{aligned} \tag{32}$$

where $C_{min}$ is the minimum allowable compliance, and $\mathbf{P}_{x_1}$, $\mathbf{P}_{x_2}$, and $\mathbf{P}_{x_3}$ are the consistent force vectors when the displacements are applied in the direction of the $x_1$-, $x_2$-, and $x_3$-axes, respectively. The first three constraints (compliance constraints) are imposed while the working domain is still in the linear elastic region, that is, a small displacement is prescribed, so there is no plastic deformation induced in the working domains. The volume fraction is denoted by $V(\boldsymbol{\xi})$ which is not allowed to have a value exceeding $V_f$. The volume fraction of a design is calculated as:

$$V(\boldsymbol{\xi}) = \frac{\boldsymbol{\phi}^T \widehat{\boldsymbol{\nu}}}{V_{total}}, \tag{33}$$

where $V_{total}$ is the total volume of the working domain $\Lambda$, and $\widehat{\boldsymbol{\nu}}$ denotes the vector of element volumes.

## 4.4 | Sensitivity analysis

Since the number of design variables in the topology optimization problem is large, the adjoint method[36,94] is employed to calculate the sensitivities. We start with a generic objective function $G(\widetilde{\mathbf{y}}^M, \dots, \widetilde{\mathbf{y}}^1, \mathbf{v}^M, \dots, \mathbf{v}^1, \boldsymbol{\phi})$ which is a function of the element density vector, unknown vector $\widetilde{\mathbf{y}}^n = \begin{bmatrix} \mathbf{u}_f^n & \mathbf{P}_a^n & \boldsymbol{\theta}^n \end{bmatrix}$, and auxiliary state variables $\mathbf{v}^n$. For the sake of brevity, we define variable $\mathbf{y}^n$ as combination of the unknown displacements (displacements at free degrees of freedom $\mathbf{u}_f^n$) and unknown forces (forces corresponding to the degrees of freedom with prescribed displacements $\mathbf{P}_a^n$), that is, $\mathbf{y}^n = \begin{bmatrix} \mathbf{u}_f^n & \mathbf{P}_a^n \end{bmatrix}$. The subscripts $f$ and $a$ correspond to degrees of freedom associated with free and prescribed displacements, respectively. The augmented objective functional $\widehat{F}$ is expressed as

$$\begin{aligned} \widehat{F}(\boldsymbol{\phi}) = G &- \sum_{n=1}^{M} \lambda^{n^T} \mathbf{R}^n \left( \widetilde{\mathbf{y}}^n, \widetilde{\mathbf{y}}^{n-1}, \mathbf{v}^n, \mathbf{v}^{n-1}, \boldsymbol{\phi} \right) \\ &- \sum_{n=1}^{M} \boldsymbol{\omega}^{n^T} \mathbf{H}^n \left( \widetilde{\mathbf{y}}^n, \widetilde{\mathbf{y}}^{n-1}, \mathbf{v}^n, \mathbf{v}^{n-1}, \boldsymbol{\phi} \right) \end{aligned} \tag{34}$$

where $\boldsymbol{\lambda}^n$ and $\boldsymbol{\omega}^n$ are arbitrary Lagrange multipliers corresponding to the residuals $\mathbf{R}^n$ and $\mathbf{H}^n$, respectively. The residuals have the property that $\mathbf{R}^n = \mathbf{0}$ and $\mathbf{H}^n = \mathbf{0}$; thus, the original and augmented objective functions are equal, and therefore their sensitivities are equal everywhere within the working domain, that is, ${}^{dG}/_{d\boldsymbol{\phi}} = {}^{d\widehat{F}}/_{d\boldsymbol{\phi}}$. The derivative ${}^{d\widehat{F}}/_{d\boldsymbol{\phi}}$, using the chain rule and reordering the terms, can be written as follows

$$\begin{aligned} \frac{d\widehat{F}}{d\boldsymbol{\phi}} &= \frac{dG}{d\boldsymbol{\phi}} - \sum_{n=1}^{M} \lambda^{n^T} \frac{d\mathbf{R}^n}{d\boldsymbol{\phi}} - \sum_{n=1}^{M} \boldsymbol{\omega}^{n^T} \frac{d\mathbf{H}^n}{d\boldsymbol{\phi}} \\ &= \frac{\partial G}{\partial \boldsymbol{\phi}} - \sum_{n=1}^{M} \left( \lambda^{n^T} \frac{\partial \mathbf{R}^n}{\partial \boldsymbol{\phi}} + \boldsymbol{\omega}^{n^T} \frac{\partial \mathbf{H}^n}{\partial \boldsymbol{\phi}} \right) \\ &\quad + \left( \frac{\partial G}{\partial \widetilde{\mathbf{y}}^M} - \lambda^{M^T} \frac{\partial \mathbf{R}^M}{\partial \widetilde{\mathbf{y}}^M} - \boldsymbol{\omega}^{M^T} \frac{\partial \mathbf{H}^M}{\partial \widetilde{\mathbf{y}}^M} \right) \frac{d\widetilde{\mathbf{y}}^M}{d\boldsymbol{\phi}} \end{aligned}$$

$$
\begin{aligned}
&+\sum_{n=1}^{M-1}\left(\frac{\partial G}{\partial \widetilde{\mathbf{y}}^n}-\boldsymbol{\lambda}^{n+1^T}\frac{\partial \mathbf{R}^{n+1}}{\partial \widetilde{\mathbf{y}}^n}-\boldsymbol{\omega}^{n+1^T}\frac{\partial \mathbf{H}^{n+1}}{\partial \widetilde{\mathbf{y}}^n}-\boldsymbol{\lambda}^{n^T}\frac{\partial \mathbf{R}^{n}}{\partial \widetilde{\mathbf{y}}^n}-\boldsymbol{\omega}^{n^T}\frac{\partial \mathbf{H}^{n}}{\partial \widetilde{\mathbf{y}}^n}\right)\frac{d\widetilde{\mathbf{y}}^n}{d\boldsymbol{\phi}}\\
&+\left(\frac{\partial G}{\partial \mathbf{v}^M}-\boldsymbol{\lambda}^{M^T}\frac{\partial \mathbf{R}^{M}}{\partial \mathbf{v}^M}-\boldsymbol{\omega}^{M^T}\frac{\partial \mathbf{H}^{M}}{\partial \mathbf{v}^M}\right)\frac{d\mathbf{v}^M}{d\boldsymbol{\phi}}\\
&+\sum_{n=1}^{M-1}\left(\frac{\partial G}{\partial \mathbf{v}^n}-\boldsymbol{\lambda}^{n+1^T}\frac{\partial \mathbf{R}^{n+1}}{\partial \mathbf{v}^n}-\boldsymbol{\omega}^{n+1^T}\frac{\partial \mathbf{H}^{n+1}}{\partial \mathbf{v}^n}-\boldsymbol{\lambda}^{n^T}\frac{\partial \mathbf{R}^{n}}{\partial \mathbf{v}^n}-\boldsymbol{\omega}^{n^T}\frac{\partial \mathbf{H}^{n}}{\partial \mathbf{v}^n}\right)\frac{d\mathbf{v}^n}{d\boldsymbol{\phi}}.
\end{aligned}
\tag{35}
$$

The calculation of the implicit derivatives $^{d\mathbf{y}^n}/_{d\boldsymbol{\phi}}$ and $^{d\mathbf{v}^n}/_{d\boldsymbol{\phi}}$ can be circumvented by choosing the Lagrange multipliers $\boldsymbol{\lambda}^n$ and $\boldsymbol{\omega}^n$ such that all terms containing $^{d\widetilde{\mathbf{y}}^n}/_{d\boldsymbol{\phi}}$ and $^{d\mathbf{v}^n}/_{d\boldsymbol{\phi}}$ sum to zero. Having said that, the Lagrange multipliers are computed in reverse chronological order, starting from the last step and ending with the first step.

$$
\begin{aligned}
&\overbrace{\begin{aligned}
&\frac{\partial G}{\partial \widetilde{\mathbf{y}}^M}-\boldsymbol{\lambda}^{M^T}\frac{\partial \mathbf{R}^{M}}{\partial \widetilde{\mathbf{y}}^M}-\boldsymbol{\omega}^{M^T}\frac{\partial \mathbf{H}^{M}}{\partial \widetilde{\mathbf{y}}^M}=\mathbf{0}\\
&\frac{\partial G}{\partial \mathbf{v}^M}-\boldsymbol{\lambda}^{M^T}\frac{\partial \mathbf{R}^{M}}{\partial \mathbf{v}^M}-\boldsymbol{\omega}^{M^T}\frac{\partial \mathbf{H}^{M}}{\partial \mathbf{v}^M}=\mathbf{0}
\end{aligned}}^{\text{Mth step:}}\\
&\overbrace{\begin{aligned}
&\frac{\partial G}{\partial \widetilde{\mathbf{y}}^n}-\boldsymbol{\lambda}^{n+1^T}\frac{\partial \mathbf{R}^{n+1}}{\partial \widetilde{\mathbf{y}}^n}-\boldsymbol{\omega}^{n+1^T}\frac{\partial \mathbf{H}^{n+1}}{\partial \widetilde{\mathbf{y}}^n}-\boldsymbol{\lambda}^{n^T}\frac{\partial \mathbf{R}^{n}}{\partial \widetilde{\mathbf{y}}^n}-\boldsymbol{\omega}^{n^T}\frac{\partial \mathbf{H}^{n}}{\partial \widetilde{\mathbf{y}}^n}=\mathbf{0}\\
&\frac{\partial G}{\partial \mathbf{v}^n}-\boldsymbol{\lambda}^{n+1^T}\frac{\partial \mathbf{R}^{n+1}}{\partial \mathbf{v}^n}-\boldsymbol{\omega}^{n+1^T}\frac{\partial \mathbf{H}^{n+1}}{\partial \mathbf{v}^n}-\boldsymbol{\lambda}^{n^T}\frac{\partial \mathbf{R}^{n}}{\partial \mathbf{v}^n}-\boldsymbol{\omega}^{n^T}\frac{\partial \mathbf{H}^{n}}{\partial \mathbf{v}^n}=\mathbf{0}
\end{aligned}}^{\text{nth step, n=M-1, … ,1}}
\end{aligned}
\tag{36}
$$

Hence, the derivative $^{d\widehat{F}}/_{d\boldsymbol{\phi}}$ reduces to

$$
\frac{dG}{d\boldsymbol{\phi}}=\frac{d\widehat{F}}{d\boldsymbol{\phi}}=\frac{\partial G}{\partial \boldsymbol{\phi}}-\sum_{n=1}^{M}\left(\boldsymbol{\lambda}^{n^T}\frac{\partial \mathbf{R}^{n}}{\partial \boldsymbol{\phi}}+\boldsymbol{\omega}^{n^T}\frac{\partial \mathbf{H}^{n}}{\partial \boldsymbol{\phi}}\right),
\tag{37}
$$

where the Lagrange multipliers $\boldsymbol{\lambda}^n$ and $\boldsymbol{\omega}^n$ are calculated using Equation (36). Note that density filtering (Equation 24) is employed to resolve numerical instabilities as discussed in Section 4.1. Obtaining the derivative with respect to the design variable $\boldsymbol{\xi}$ is trivial, and it only requires a straightforward implementation of the chain rule

$$
\frac{dG}{d\xi}=\frac{dG}{d\boldsymbol{\phi}}\frac{d\boldsymbol{\phi}}{d\xi}=\frac{dG}{d\boldsymbol{\phi}}\overline{\boldsymbol{W}}.
\tag{38}
$$

In the context of the adopted constitutive model, the global equilibrium residual vector $\mathbf{R}_1^n$ is expressed as

$$
\begin{aligned}
\mathbf{R}_1^n&=\overset{N_{ele}}{\underset{e=1}{\mathscr{A}}}\left(\sum_{\text{Gauss points } r}\mathbf{R}_r^n\right),\\
\mathbf{R}_r^n&=\mathbf{B}^T\boldsymbol{\sigma}^T wJ-\mathbf{N}^T\mathbf{b}^n wJ-\mathbf{N}^T\mathbf{t}^n wj,
\end{aligned}
\tag{39}
$$

where $\mathbf{N}$ and $\mathbf{B}$ are the usual shape function matrix and shape function derivative matrix, respectively. Also, $w$ denotes the weighting function while $J$ and $j$ denote the volume and area metrics. In the present work, we assume there is no body force, that is, $\mathbf{b}^n=0$, and each element has eight Gauss points ($r=1,\ \dots,8$). The auxiliary variable state $\mathbf{v}^n$ is defined at each Gauss point as follows

$$
\begin{aligned}
\mathbf{v}^n&=[\boldsymbol{\sigma}^n]\ \text{ elastic loading or unloading,}\\
\mathbf{v}^n&=\begin{bmatrix}\boldsymbol{\varepsilon}^{p^n}\\ \alpha^n\\ \boldsymbol{\sigma}^n\\ \gamma^n\end{bmatrix}\ \text{plastic loading.}
\end{aligned}
\tag{40}
$$

The residual $\mathbf{H}^n$ is defined at each Gauss point. In the case of elastic loading or unloading, $\mathbf{H}^n$ is

$$\mathbf{H}^n = \boldsymbol{\sigma}^{n-1} + \mathbf{C}^{el}\left(\mathbf{B}\mathbf{u}^n - \mathbf{B}\mathbf{u}^{n-1}\right) - \boldsymbol{\sigma}^n = \mathbf{0}, \tag{41}$$

where $\mathbf{C}^{el}$ is the elastic constitutive matrix. In the case of plastic loading, $\mathbf{H}^n$ is

$$\mathbf{H}^n = \begin{bmatrix} \mathbf{H}^n_{\boldsymbol{\varepsilon}^p} \\ \mathrm{H}^n_{\alpha} \\ \mathbf{H}^n_{\boldsymbol{\sigma}} \\ \mathrm{H}^n_{\gamma} \end{bmatrix} = \mathbf{0}, \tag{42}$$

where

$$\begin{aligned} \mathbf{H}^n_{\boldsymbol{\varepsilon}^p} &= \boldsymbol{\varepsilon}^{p^{n-1}} + \left(\gamma^n - \gamma^{n-1}\right)\mathbf{n} - \boldsymbol{\varepsilon}^{p^n}, \\ \mathrm{H}^n_{\alpha} &= \alpha^{n-1} + \sqrt{2/3}\,\left(\gamma^n - \gamma^{n-1}\right) - \alpha^n, \\ \mathbf{H}^n_{\boldsymbol{\sigma}} &= \boldsymbol{\sigma}^{n-1} + \mathbf{C}^{el}\left(\mathbf{B}\mathbf{u}^n - \mathbf{B}\mathbf{u}^{n-1} - \boldsymbol{\varepsilon}^{p^n} + \boldsymbol{\varepsilon}^{p^{n-1}}\right) - \boldsymbol{\sigma}^n, \\ \mathrm{H}^n_{\gamma} &= \|\mathbf{s}\| - \sqrt{2/3}(\sigma_{y_e} + K_e\,\alpha). \end{aligned} \tag{43}$$

Using Equations (26) and (28), the explicit derivatives of $G$ required in the optimization procedure are evaluated as

$$\begin{aligned} \frac{\partial G}{\partial \boldsymbol{\phi}} &= \mathbf{0}, \\ \frac{\partial G}{\partial \mathbf{v}^n} &= \mathbf{0}. \end{aligned} \tag{44}$$

Next, we define the explicit derivative of $G$ with respect to $\widetilde{\mathbf{y}}^n = \begin{bmatrix}\mathbf{y}^n & \boldsymbol{\theta}^n\end{bmatrix}$ in the case of toughness and end compliance. Starting with toughness, the components of $\frac{\partial G_{toughness}}{\partial \widetilde{\mathbf{y}}^n}$ are expressed as

$$\begin{aligned} \frac{\partial G_{toughness}}{\partial \boldsymbol{\theta}^n} &= \mathbf{0}, \\ \frac{\partial G_{toughness}}{\partial \mathbf{y}^n} &= \sum_{n=1}^{M} \frac{\partial F_n}{\partial \mathbf{y}^n}, \quad \frac{\partial F_n}{\partial \mathbf{y}^n} = \boldsymbol{L}^T \frac{\partial \mathbf{P}_n}{\partial \mathbf{y}^n}, \\ \frac{\partial \mathbf{P}_n}{\partial \mathbf{y}^n} &= \begin{bmatrix} \mathbf{0}_{ff} & \mathbf{0}_{fa} \\ \mathbf{0}_{af} & I_{aa} \end{bmatrix}, \end{aligned} \tag{45}$$

where $I$ is the identity matrix. In the case of maximizing the end compliance, the derivative of $G$ with respect to $\widetilde{\mathbf{y}}^n$ is written as

$$\begin{aligned} &\frac{\partial G_{end\ compliance}}{\partial \boldsymbol{\theta}^n} = \mathbf{0} \quad for \quad n \le M, \\ &\frac{\partial G_{end\ compliance}}{\partial \mathbf{y}^n} = \mathbf{0} \quad for \quad n \le M-1, \quad \frac{\partial G_{end\ compliance}}{\partial \mathbf{y}^M} = \begin{bmatrix} \mathbf{0}_f \\ \mathbf{u}_a^T \end{bmatrix}_M. \end{aligned} \tag{46}$$

Given Equations (39) and (40), the explicit derivatives of $\mathbf{R}^n$ with respect to $\boldsymbol{\phi}, \widetilde{\mathbf{y}}^n, \widetilde{\mathbf{y}}^{n-1}, \mathbf{v}^n$, and $\mathbf{v}^{n-1}$ are obtained from the equation below

$$\begin{aligned} \frac{\partial \mathbf{R}^n}{\partial \boldsymbol{\phi}} &= \mathbf{0}, \quad \frac{\partial \mathbf{R}^n}{\partial \widetilde{\mathbf{y}}^{n-1}} = \mathbf{0}, \\ \frac{\partial \mathbf{R}^n}{\partial \mathbf{v}^{n-1}} &= \mathbf{0}, \quad \frac{\partial \mathbf{R}^n}{\partial \mathbf{v}^n} = \begin{bmatrix}\mathbf{0} & \mathbf{0} & \mathbf{B}^T w J & \mathbf{0}\end{bmatrix}, \end{aligned}$$

$$\frac{\partial \mathbf{R}^n}{\partial \mathbf{y}^n} = \begin{bmatrix} \mathbf{0}_{ff} & \mathbf{0}_{fa} \\ \mathbf{0}_{af} & -I_{aa} \end{bmatrix}, \quad \frac{\partial \mathbf{R}^n}{\partial \widetilde{\mathbf{y}}^n} = \begin{bmatrix} \frac{\partial \mathbf{R}^n}{\partial \mathbf{y}^n} & -\mathbf{A}^T \\ \mathbf{A} & \mathbf{0} \end{bmatrix}. \tag{47}$$

The explicit derivative of $\mathbf{H}^n$ with respect to $\boldsymbol{\phi}$ is expressed as

$$\frac{\partial \mathbf{H}^n}{\partial \boldsymbol{\phi}} = \left[\frac{\partial \mathbf{C}^{el}}{\partial \boldsymbol{\phi}} \left(\mathbf{B}\mathbf{u}^n - \mathbf{B}\mathbf{u}^{n-1}\right)\right] \text{ elastic loading,}$$
$$\frac{\partial \mathbf{H}^n}{\partial \boldsymbol{\phi}} = \begin{bmatrix} \mathbf{0} \\ \mathbf{0} \\ \frac{\partial \mathbf{C}^{el}}{\partial \boldsymbol{\phi}} \left(\mathbf{B}\mathbf{u}^n - \mathbf{B}\mathbf{u}^{n-1} - \boldsymbol{\varepsilon}^{p^n} + \boldsymbol{\varepsilon}^{p^{n-1}}\right) \\ -\sqrt{2/3} \left(\frac{\partial \sigma_{y_e}}{\partial \boldsymbol{\phi}} + \frac{\partial K_e}{\partial \boldsymbol{\phi}} \alpha\right) \end{bmatrix} \text{ plastic loading,} \tag{48}$$

where

$$\frac{\partial \mathbf{C}^{el}}{\partial \boldsymbol{\phi}} = p_1 (E - E_{min}) \phi_e^{(p_1 - 1)} \mathbf{C}^o,$$
$$\frac{\partial \sigma_{y_e}}{\partial \boldsymbol{\phi}} = p_2 (\sigma_y - \sigma_{y_{min}}) \phi_e^{(p_2 - 1)},$$
$$\frac{\partial K_e}{\partial \boldsymbol{\phi}} = p_3 (K - K_{min}) \phi_e^{(p_3 - 1)}, \tag{49}$$

where $\mathbf{C}^o$ is the elasticity tensor evaluated with $\phi_e = 1 (E_e = E)$. The explicit derivatives of $\mathbf{H}^n$ with respect to $\widetilde{\mathbf{y}}^n$ and $\widetilde{\mathbf{y}}^{n-1}$ are

$$\frac{\partial \mathbf{H}^n}{\partial \boldsymbol{\theta}^n} = \frac{\partial \mathbf{H}^n}{\partial \boldsymbol{\theta}^{n-1}} = \mathbf{0}, \quad \frac{\partial \mathbf{H}^n}{\partial \mathbf{y}^n} = \begin{bmatrix} \mathbf{0} \\ \mathbf{0} \\ \frac{\partial \mathbf{H}_{\boldsymbol{\sigma}}^n}{\partial \mathbf{y}^n} \\ \mathbf{0} \end{bmatrix}, \quad \frac{\partial \mathbf{H}^n}{\partial \mathbf{y}^{n-1}} = \begin{bmatrix} \mathbf{0} \\ \mathbf{0} \\ \frac{\partial \mathbf{H}_{\boldsymbol{\sigma}}^n}{\partial \mathbf{y}^{n-1}} \\ \mathbf{0} \end{bmatrix}, \tag{50}$$

where $\frac{\partial \mathbf{H}_{\boldsymbol{\sigma}}^n}{\partial \mathbf{y}^n} = \mathbf{C}^{el}\mathbf{B}$ and $\frac{\partial \mathbf{H}_{\boldsymbol{\sigma}}^n}{\partial \mathbf{y}^{n-1}} = -\mathbf{C}^{el}\mathbf{B}$ at free degrees of freedom, and $\frac{\partial \mathbf{H}_{\boldsymbol{\sigma}}^n}{\partial \mathbf{y}^n} = \frac{\partial \mathbf{H}_{\boldsymbol{\sigma}}^n}{\partial \mathbf{y}^{n-1}} = \mathbf{0}$ at prescribed degrees of freedom. In the case of elastic loading, $\frac{\partial \mathbf{H}^n}{\partial \mathbf{y}^n}$ and $\frac{\partial \mathbf{H}^n}{\partial \mathbf{y}^{n-1}}$ are reduced to

$$\frac{\partial \mathbf{H}^n}{\partial \mathbf{y}^{n-1}} = \frac{\partial \mathbf{H}_{\boldsymbol{\sigma}}^n}{\partial \mathbf{y}^{n-1}}, \quad \frac{\partial \mathbf{H}^n}{\partial \mathbf{y}^n} = \frac{\partial \mathbf{H}_{\boldsymbol{\sigma}}^n}{\partial \mathbf{y}^n}. \tag{51}$$

The derivative of $\mathbf{H}^n$ with respect to $\mathbf{v}^{n-1}$ is

$$\frac{\partial \mathbf{H}^n}{\partial \mathbf{v}^{n-1}} = I \text{ elastic loading,}$$
$$\frac{\partial \mathbf{H}^n}{\partial \mathbf{v}^{n-1}} = \begin{bmatrix} I & \mathbf{0} & \mathbf{0} & -\mathbf{n} \\ \mathbf{0} & 1 & \mathbf{0} & -\sqrt{2/3} \\ \mathbf{C}^{el} & \mathbf{0} & I & \mathbf{0} \\ \mathbf{0} & 0 & \mathbf{0} & 0 \end{bmatrix} \text{ plastic loading.} \tag{52}$$

Finally, the derivative of $\mathbf{H}^n$ with respect to $\mathbf{v}^n$ is

$$\frac{\partial \mathbf{H}^n}{\partial \mathbf{v}^n} = -I \text{ elastic loading,}$$

$$\frac{\partial \mathbf{H}^n}{\partial \mathbf{v}^n} = \begin{bmatrix} -I & \mathbf{0} & \left(\gamma^n - \gamma^{n-1}\right)\frac{\partial \mathbf{n}}{\partial \boldsymbol{\sigma}} & \mathbf{n} \\ \mathbf{0} & -1 & \mathbf{0} & \sqrt{2/3} \\ -\mathbf{C}^{el} & \mathbf{0} & -I & \mathbf{0} \\ \mathbf{0} & -\sqrt{2/3}K_e & \mathbf{n} & 0 \end{bmatrix} \text{ plastic loading,} \tag{53}$$

where

$$\frac{\partial \mathbf{n}}{\partial \boldsymbol{\sigma}} = \frac{1}{\|\mathbf{s}\|}\left(\mathbf{I} - \frac{1}{3}\mathbf{1}\otimes\mathbf{1} - \mathbf{n}\otimes\mathbf{n}\right). \tag{54}$$

Below is a summary for the mathematical framework used here

$$\begin{aligned} \frac{dG}{d\boldsymbol{\xi}} &= \frac{dG}{d\boldsymbol{\phi}}\frac{d\boldsymbol{\phi}}{d\boldsymbol{\xi}} = \frac{dG}{d\boldsymbol{\phi}}\overline{\boldsymbol{W}}, \\ \frac{dG}{d\boldsymbol{\phi}} &= \frac{d\widehat{F}}{d\boldsymbol{\phi}} = -\sum_{n=1}^{M}\left(\boldsymbol{\omega}^{n^T}\frac{\partial \mathbf{H}^n}{\partial \boldsymbol{\phi}}\right), \end{aligned} \tag{55}$$

where $\boldsymbol{\omega}^n$ in the case of toughness maximization is calculated as

$$\overbrace{\begin{gathered}\left(\frac{\partial \mathbf{R}^M}{\partial \widetilde{\mathbf{y}}^M} - \frac{\partial \mathbf{R}^M}{\partial \mathbf{v}^M}\left(\frac{\partial \mathbf{H}^M}{\partial \mathbf{v}^M}\right)^{-1}\frac{\partial \mathbf{H}^M}{\partial \widetilde{\mathbf{y}}^M}\right)^T \lambda^M = \frac{\partial F_M}{\partial \widetilde{\mathbf{y}}^M} \\ \boldsymbol{\omega}^M = -\left(\frac{\partial \mathbf{H}^M}{\partial \mathbf{v}^M}\right)^{-T}\left(\frac{\partial \mathbf{R}^M}{\partial \mathbf{v}^M}\right)^T \lambda^M\end{gathered}}^{\text{Mth step:}}$$

$$\overbrace{\begin{gathered}\left(\frac{\partial \mathbf{R}^n}{\partial \widetilde{\mathbf{y}}^n} - \frac{\partial \mathbf{R}^n}{\partial \mathbf{v}^n}\left(\frac{\partial \mathbf{H}^n}{\partial \mathbf{v}^n}\right)^{-1}\frac{\partial \mathbf{H}^n}{\partial \widetilde{\mathbf{y}}^n}\right)^T \lambda^n = \frac{\partial F_n}{\partial \widetilde{\mathbf{y}}^n} - \left(\frac{\partial \mathbf{H}^{n+1}}{\partial \widetilde{\mathbf{y}}^n} - \frac{\partial \mathbf{H}^{n+1}}{\partial \mathbf{v}^n}\left(\frac{\partial \mathbf{H}^n}{\partial \mathbf{v}^n}\right)^{-1}\frac{\partial \mathbf{H}^n}{\partial \widetilde{\mathbf{y}}^n}\right)^T \boldsymbol{\omega}^{n+1} \\ \boldsymbol{\omega}^n = -\left(\frac{\partial \mathbf{H}^n}{\partial \mathbf{v}^n}\right)^{-T}\left(\left(\frac{\partial \mathbf{R}^n}{\partial \mathbf{v}^n}\right)^T \lambda^n + \left(\frac{\partial \mathbf{H}^{n+1}}{\partial \mathbf{v}^n}\right)^T \boldsymbol{\omega}^{n+1}\right)\end{gathered}}^{\text{nth step, n=M-1, … ,1}}, \tag{56}$$

while in the case of end compliance maximization, $\boldsymbol{\omega}^n$ is evaluated using

$$\overbrace{\begin{gathered}\left(\frac{\partial \mathbf{R}^M}{\partial \widetilde{\mathbf{y}}^M} - \frac{\partial \mathbf{R}^M}{\partial \mathbf{v}^M}\left(\frac{\partial \mathbf{H}^M}{\partial \mathbf{v}^M}\right)^{-1}\frac{\partial \mathbf{H}^M}{\partial \widetilde{\mathbf{y}}^M}\right)^T \lambda^M = \frac{\partial G_{end\ compliance}}{\partial \widetilde{\mathbf{y}}^M} \\ \boldsymbol{\omega}^M = -\left(\frac{\partial \mathbf{H}^M}{\partial \mathbf{v}^M}\right)^{-T}\left(\frac{\partial \mathbf{R}^M}{\partial \mathbf{v}^M}\right)^T \lambda^M\end{gathered}}^{\text{Mth step:}}$$

$$\overbrace{\begin{gathered}\left(\frac{\partial \mathbf{R}^n}{\partial \widetilde{\mathbf{y}}^n} - \frac{\partial \mathbf{R}^n}{\partial \mathbf{v}^n}\left(\frac{\partial \mathbf{H}^n}{\partial \mathbf{v}^n}\right)^{-1}\frac{\partial \mathbf{H}^n}{\partial \widetilde{\mathbf{y}}^n}\right)^T \lambda^n = -\left(\frac{\partial \mathbf{H}^{n+1}}{\partial \widetilde{\mathbf{y}}^n} - \frac{\partial \mathbf{H}^{n+1}}{\partial \mathbf{v}^n}\left(\frac{\partial \mathbf{H}^n}{\partial \mathbf{v}^n}\right)^{-1}\frac{\partial \mathbf{H}^n}{\partial \widetilde{\mathbf{y}}^n}\right)^T \boldsymbol{\omega}^{n+1} \\ \boldsymbol{\omega}^n = -\left(\frac{\partial \mathbf{H}^n}{\partial \mathbf{v}^n}\right)^{-T}\left(\left(\frac{\partial \mathbf{R}^n}{\partial \mathbf{v}^n}\right)^T \lambda^n + \left(\frac{\partial \mathbf{H}^{n+1}}{\partial \mathbf{v}^n}\right)^T \boldsymbol{\omega}^{n+1}\right)\end{gathered}}^{\text{nth step,n=M-1, … ,1}}. \tag{57}$$

The required matrices are provided in Equations (44)–(54). The sensitivities of the volume and elastic compliance constraints are straightforward and available in many papers, and we do not include them for the sake of conciseness.

Error-free implementation of the sensitivities discussed above is not a trivial task. We ensure that the analytical sensitivities of the objective function and constraints are correctly implemented by comparing them with those obtained from the central finite difference (CFD) method. A cube with 64 elements, where all elements possess a uniform density (0.5, which is equivalent to the volume constraint used in the following section), is considered as the

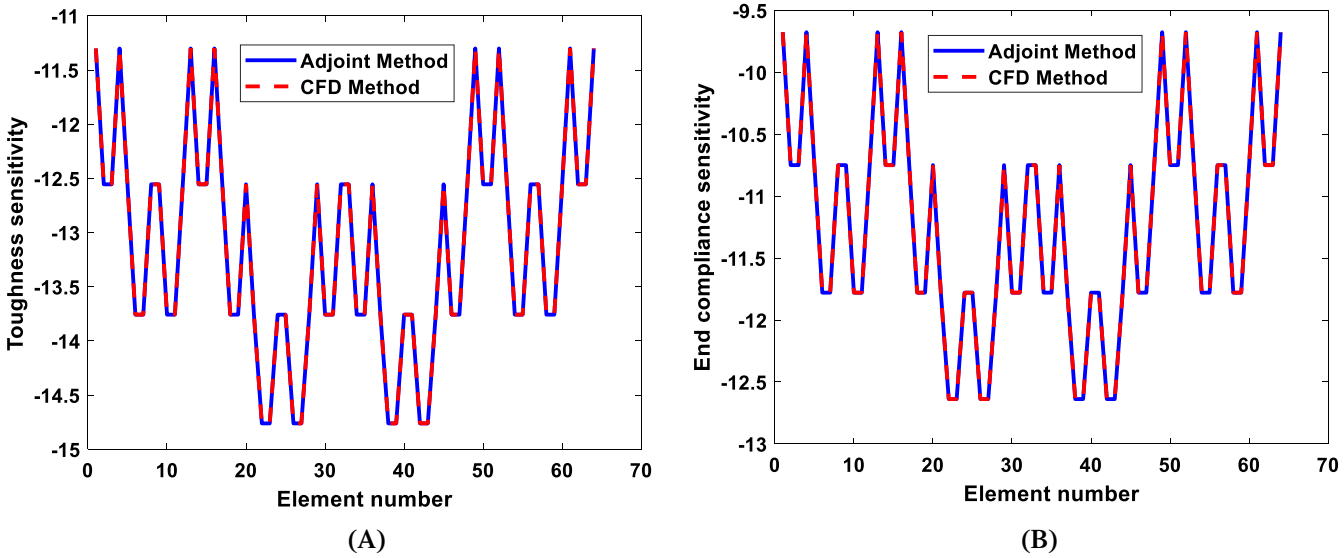


**FIGURE 3** Sensitivity comparison results: (A) Toughness (unit: kJ/m$^3$), (B) end compliance (unit: N·mm). CFD method refers to the central finite difference method. The length of the cube unit cell is 10 mm

verification model. A uniaxial compressive strain (2% applied strain, which is large enough to induce plastic deformation given the low densities of the elements) is applied. Figure 3 shows two examples of sensitivity verification analysis.

## 5 | RESULTS AND DISCUSSION

In this section, the elastoplastic optimization procedure described above is implemented to maximize either toughness or end compliance, where the framework is demonstrated on 3D example problems. The elements chosen for the analysis are eight-node hexahedral elements, where an eight-point Gaussian quadrature rule is used for numerical integration. The working domain $\Lambda$ is a bulk cube (see Figure 4(A)). We start by running a finite element analysis for the working domain under a specific applied strain to ensure that its response is insensitive to the number of elements used in the analysis. The mesh sensitivity study is shown in Figure 4(B), where a uniaxial strain of 5% is applied for the three meshes of $\Lambda$. Figure 4(B) indicates that 8000 elements are acceptable given the high computational cost of the optimization procedure; hence, this number is chosen for the optimization problem.

The optimization algorithm is implemented in MATLAB. The optimization problems, along with the finite element analyses, have been run on a parallel cluster, using 16 Skylake cores and 128 GB RAM. The optimization procedure is performed using one unit cell, called representative unit cell (RUC), without imposing symmetry constraints[95-97] within the unit cell. Additionally, buckling and damage are key physical considerations for the design of cellular materials for many engineering applications. In this study, the effects of damage and buckling are not directly accounted for, and we assume that the stress levels are not high enough to induce either phenomenon. The present topology optimization problem is solved using the method of moving asymptotes (MMA).[98] The MMA method is a gradient-based optimization method that is efficient at solving large-scale constrained optimization problems by solving a sequence of convex subproblems. The convergence tolerance for the optimization task is $\varepsilon_{opt} \leq 10^{-5}$. For each displacement increment, the Newton–Raphson equation is solved to a tolerance of $\varepsilon_{NR} \leq 10^{-8}$. The material properties used in this article are: bulk modulus $\kappa = 7.33$ GPa, shear modulus $\mu = 4.40$ GPa, initial yield stress $\sigma_y = 120$ MPa, and hardening modulus $K = 900$ MPa. With regard to Equation (32), the minimum admissible compliance per unit volume for all optimized materials is $C_{min} = 200$ N·m/m$^3$. For all optimization problem discussed below, we use a continuation scheme for the penalization factor. More specifically, the penalty factors are increased from $p_1 = p_2 = p_3 = 1$ to $p_1 = p_2 = p_3 = 3$. For the first 10 optimization iterations, $p_1 = p_2 = p_3 = 1$, and then $p_1$, $p_2$, and $p_3$ are increased by 2% from the previous iteration until $p_1 = p_2 = p_3 = 3$.

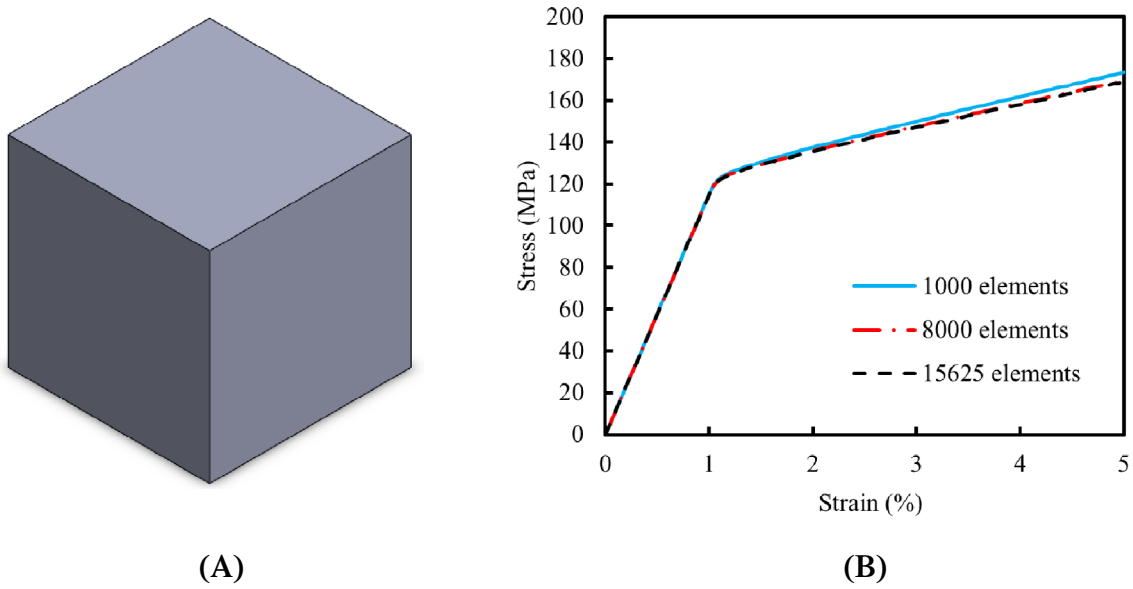


**FIGURE 4** Illustration of (A) the working domain used in the study, and (B) its mesh sensitivity study

For macroscopic structural optimization problems, one can use a uniform density distribution for the initial design, as the corresponding initial displacement field is nonuniform throughout the working domain due to the nature of the loading, boundary conditions, and geometry. Using an initial design with uniform densities helps avoid any predefined designs that steer the optimizer into a specific local optimum. The nonuniform displacement field induces nonuniform sensitivities utilized by the optimizer to attain the next design point in the design space. However, this is not the case for a homogenized working domain, as an initial uniform density design will result in a uniform strain throughout the domain and hence uniform sensitivities which cause the optimizer to fail. This problem can be overcome by introducing a nonuniform initial density distribution or defining some elements as passive. Passive elements are elements in the working domain that are not allowed to have a density larger than a predefined threshold (e.g., 0.001). These two approaches will bias the optimizer into a local minimum.

To illustrate this point, the working domain $\Lambda$, with 1000 elements, is considered first before running the optimization problem for a working domain with a finer mesh. We use a coarse mesh to reduce the computational cost, yet highlight some significant aspects when dealing with periodic elastoplastic microstructures. It is subject to uniaxial compressive strain ($\overline{\varepsilon}_{11} = -2.5\%$) or pure shear ($\overline{\varepsilon}_{12} = 2.5\%$). The working domain is optimized for maximum end compliance or toughness. We use a volume constraint of $V_f = 0.5$ (i.e., porosity is 50%). We show three scenarios for the initial distribution. Firstly, we use passive elements (i.e., we enforce a void region) at the center of the working domain, where the volume fraction of the void is 0.027 (2.7%). In the second case, we enforce passive elements near the corners. The total volume fraction of the eight voids is 2.7%. Note that both scenarios of selecting the passive elements maintain the symmetry lines of the RUC along the $x_1$-, $x_2$-, and $x_3$-directions. In the third case, we do not introduce passive elements, but we use a random density distribution.

Figures 5 and 6 show the designs when the working domain is subject to uniaxial strain and optimized for toughness and end compliance, respectively. Each objective has three different scenarios: (1) passive elements at the center, (2) passive elements close to the corners, and (3) initial design with random density distribution. The RUC is not constrained to possess symmetry axes along the $x_1$-, $x_2$-, and $x_3$-directions. Nevertheless, the RUCs obtained from the first two scenarios have such symmetry lines due to the symmetric loading and initial design. Additionally, when we start with a random distribution (without defining passive elements), the symmetry lines are lost. A similar study is performed when the working domain is subject to pure shear. Figure 7 shows the RUC designs obtained using both objective functions discussed above. Figure 8 portrays the stress–strain curves for the different designs. The results discussed above, for both uniaxial and shear cases, indicate that periodic elastoplastic optimization is dependent on the location of the passive elements. This leads us to the question of which sites with passive elements one should use, as a priori knowledge of the solution could steer the optimizer to a better solution.

Finally, we show the optimization results when a working domain with a finer mesh is considered. In the context of Figure 4, we consider a mesh with 8000 elements, where we assign passive elements at the center. The passive elements

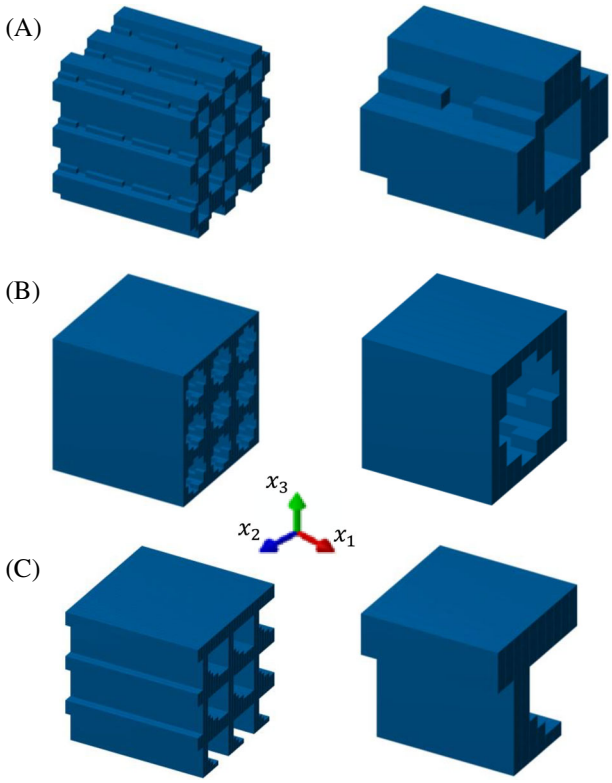


**FIGURE 5** RUC designs when optimized for toughness, the porosity is 50%, and it is subject to uniaxial strain ($\overline{\varepsilon}_{11}$): (A) passive elements at the center, (B) passive elements close to the corners, and (C) random initial distribution. The images at the leftmost column show three-dimensionally repeated cells, 27 ($3 \times 3 \times 3$) cells, and the ones at the rightmost column depict one cell

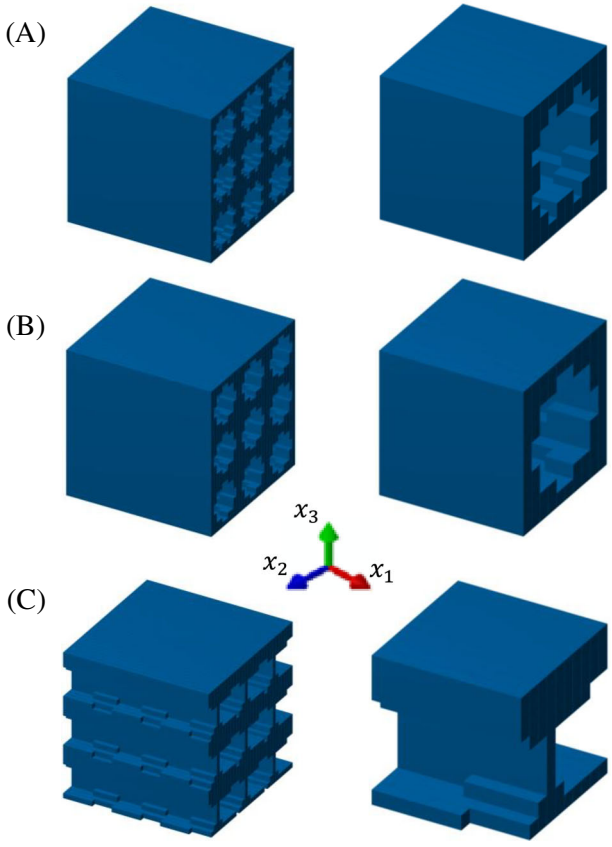


**FIGURE 6** RUC designs when optimized for end compliance, the porosity is 50%, and it is subject to uniaxial strain ($\overline{\varepsilon}_{11}$): (A) passive elements at the center, (B) passive elements close to the corners, and (C) random initial distribution. The images at the leftmost column show three-dimensionally repeated cells, 27 ($3 \times 3 \times 3$) cells, and the ones at the rightmost column depict one cell

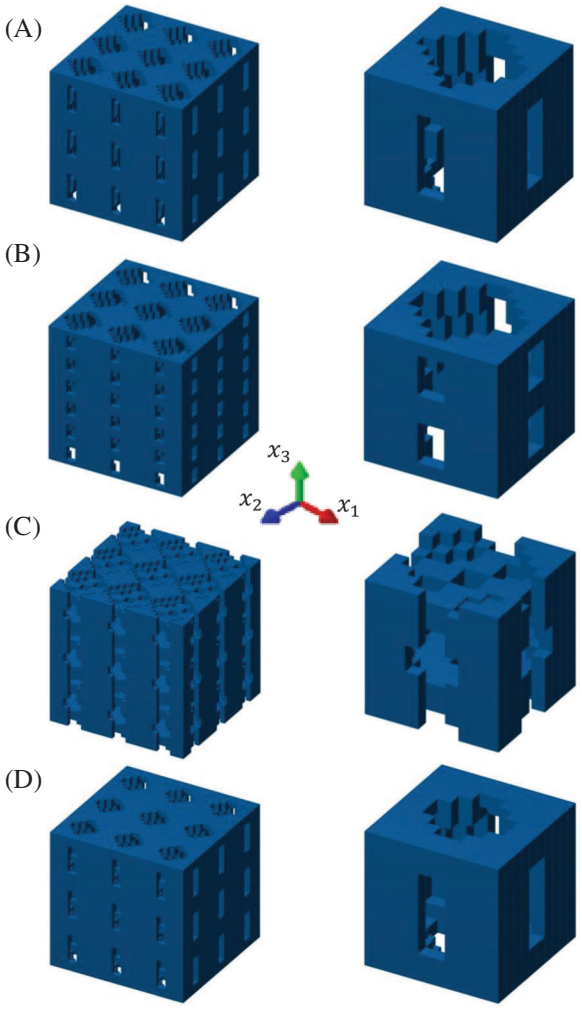


**FIGURE 7** RUC designs with a porosity of 50%, it is subject to shear strain ($\bar{\varepsilon}_{12}$), and it is optimized for (A) toughness with passive elements at the center, (B) toughness with passive elements close to the corners, (C) end compliance with passive elements at the center, and (D) end compliance with passive elements close to the corners. The images at the leftmost column show three-dimensionally repeated cells, 27 ($3 \times 3 \times 3$) cells, and the ones at the rightmost column depict one cell

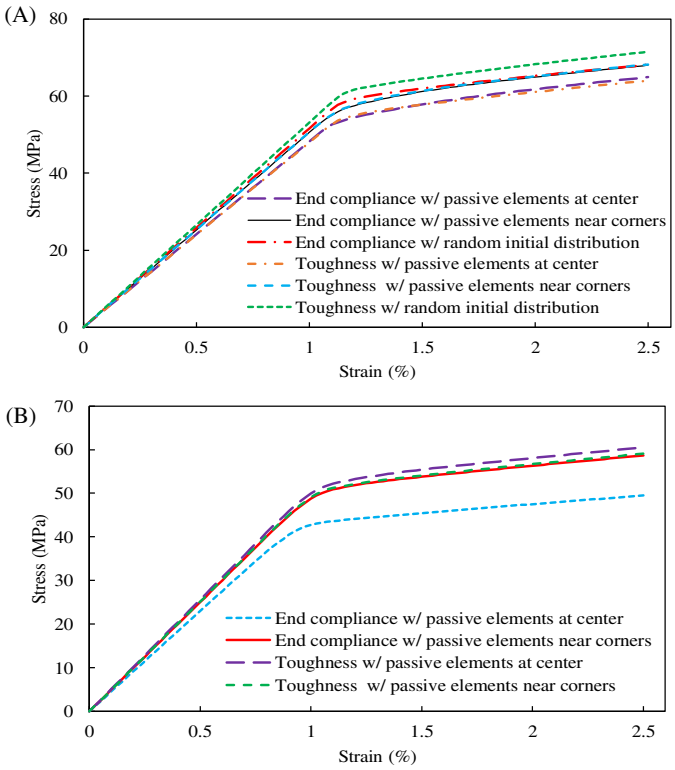


**FIGURE 8** Stress–strain curves of unit cells optimized under (A) uniaxial strain and (B) shear strain. All cells have a porosity of 50%

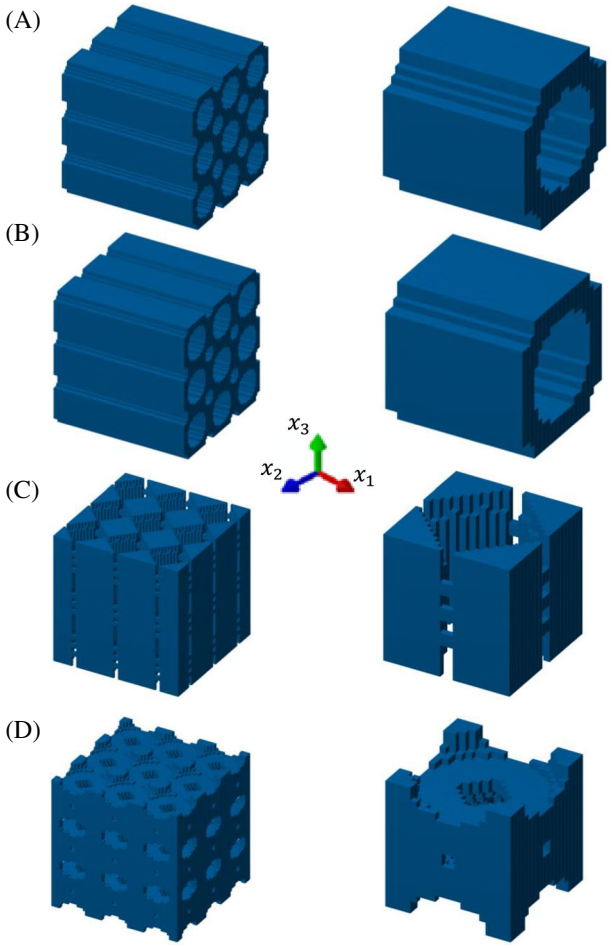


**FIGURE 9** RUC designs with a porosity of 50%. The working domain is subject to uniaxial strain ($\bar{\varepsilon}_{11}$), and it is optimized for (A) toughness and (B) end compliance. The working domain is under shear strain ($\bar{\varepsilon}_{12}$), and it is optimized for (C) toughness and (D) end compliance. The images at the leftmost column show three-dimensionally repeated cells, 27 ($3 \times 3 \times 3$) cells, and the ones at the rightmost column depict one cell

are at the center of the working domain, where the volume fraction of the void is 0.027 (2.7%). The filter radius used is 2.5 × the element size in a working domain. The working domain is subject to uniaxial compressive strain ($\bar{\varepsilon}_{11} = -2.5\%$) or pure shear strain ($\bar{\varepsilon}_{12} = 2.5\%$). For each optimization iteration, the boundary value problem is solved using 50 equal-sized increments of applied displacement. Each working domain is used to maximize the toughness and end compliance, while maintaining an end porosity of 50% for optimized RUCs. Figure 9 shows the different optimized RUCs obtained from the different objectives and loading conditions.

## 6 | CONCLUSIONS

In this study, we have proposed a framework for the design of elastoplastic materials with enhanced performance through the maximization of either toughness or end compliance. The optimization objective is to enhance the performance of an elastoplastic material obeying the von Mises plasticity model, subject to mass and elastic compliance constraints. Elastic compliance constraints help maintain the connectivity of the representative unit cell (RUC). We have derived a path-dependent adjoint method to accurately and efficiently compute the sensitivities of the objective functions and constraints. Periodic boundary conditions have been imposed using Lagrange multipliers. Also, we have studied the effect of the initial designs. In our future work, we plan to include the effect of damage and buckling phenomena, as they play a vital role in determining the mechanical properties of lattice-based materials.

## ACKNOWLEDGMENTS

This research was partially supported by the National Science Foundation (NSF) I/UCRC Center for Novel High Voltage/Temperature Materials and Structures (grant IIP-1362146), the NSF grant MOMS-1926353, and the Zhejiang University–University of Illinois at Urbana-Champaign Institute Research Program. Also, the authors would like to thank

the Industry Program at the National Center for Supercomputing Applications (NCSA) at the University of Illinois for hardware and software support. Any conclusions and results expressed in this article are merely those of the author(s) and do not imply the opinion of NSF or NCSA.

## DATA AVAILABILITY STATEMENT

The data that support the findings of this study are available from the corresponding author upon reasonable request.

## ORCID

*Diab W. Abueidda* https://orcid.org/0000-0003-3594-2455
*Kai A. James* https://orcid.org/0000-0003-2593-9762
*Iwona M. Jasiuk* https://orcid.org/0000-0001-9663-4734

## REFERENCES

1. Osanov M, Guest JK. Topology optimization for architected materials design. *Annu Rev Mat Res*. 2016;46:211-233.
2. Schaedler TA, Jacobsen AJ, Torrents A, et al. Ultralight metallic microlattices. *Science*. 2011;334(6058):962-965.
3. Abueidda DW, Karimi P, Jin J-M, Sobh NA, Jasiuk IM, Ostoja-Starzewski M. Shielding effectiveness and bandgaps of interpenetrating phase composites based on the Schwarz primitive surface. *J Appl Phys*. 2018;124(17):175102.
4. Maskery I, Sturm L, Aremu A, et al. Insights into the mechanical properties of several triply periodic minimal surface lattice structures made by polymer additive manufacturing. *Polymer*. 2018;152:62-71.
5. Al-Ketan O, Rowshan R, Palazotto AN, Al-Rub RKA. On mechanical properties of cellular steel solids with shell-like periodic architectures fabricated by selective laser sintering. *J Eng Mater Technol*. 2019;141(2):021009.
6. Barthelat F. Architectured materials in engineering and biology: fabrication, structure, mechanics and performance. *Int Mater Rev*. 2015;60(8):413-430.
7. Fleck N, Deshpande V, Ashby M. Micro-architectured materials: past, present and future. *Proc Royal Soc A Math Phys Eng Sci*. 2010;466(2121):2495-2516.
8. Abueidda DW, Elhebeary M, Shiang C-SA, Al-Rub RKA, Jasiuk IM. Compression and buckling of microarchitectured Neovius-lattice. *Extreme Mech Lett*. 2020;37:100688.
9. Al-Rub RKA, Abueidda DW, Dalaq AS. Thermo-electro-mechanical properties of interpenetrating phase composites with periodic architectured reinforcements. *From Creep Damage Mechanics to Homogenization Methods*. New York, NY: Springer; 2015:1-18.
10. Jie G, Hao L, Liang G, Mi X. Topological shape optimization of 3D micro-structured materials using energy-based homogenization method. *Adv Eng Softw*. 2018;116:89-102.
11. Christensen RM. Mechanics of cellular and other low-density materials. *Int J Solids Struct*. 2000;37(1–2):93-104.
12. van Dijk NP, Maute K, Langelaar M, Van Keulen F. Level-set methods for structural topology optimization: a review. *Struct Multidiscip Optim*. 2013;48(3):437-472.
13. Ryu Y, Haririan M, Wu C, Arora J. Structural design sensitivity analysis of nonlinear response. *Comput Struct*. 1985;21(1–2):245-255.
14. Bendsøe MP, Kikuchi N. Generating optimal topologies in structural design using a homogenization method. *Comput Methods Appl Mech Eng*. 1988;71(2):197-224.
15. Bendøse M, Sigmund O. *Topology Optimization: Theory Methods and Applications*. New York, NY: Springer; 2003.
16. Wang Y, Xu H, Pasini D. Multiscale isogeometric topology optimization for lattice materials. *Comput Methods Appl Mech Eng*. 2017;316:568-585.
17. Gogarty E, Pasini D. Hierarchical topology optimization for bone tissue scaffold: preliminary results on the design of a fracture fixation plate. *Engineering and Applied Sciences Optimization*. Cham, Switzerland: Springer; 2015:311-340.
18. Chin TW, Leader MK, Kennedy GJ. A scalable framework for large-scale 3D multimaterial topology optimization with octree-based mesh adaptation. *Adv Eng Softw*. 2019;135:102682.
19. Le C, Norato J, Bruns T, Ha C, Tortorelli D. Stress-based topology optimization for continua. *Struct Multidiscip Optim*. 2010;41(4):605-620.
20. Zhang S, Gain AL, Norato JA. Stress-based topology optimization with discrete geometric components. *Comput Methods Appl Mech Eng*. 2017;325:1-21.
21. Kollmann HT, Abueidda DW, Koric S, Guleryuz E, Sobh NA. Deep learning for topology optimization of 2D metamaterials. *Mater Des*. 2020;196:109098.
22. Gao J, Xue H, Gao L, Luo Z. Topology optimization for auxetic metamaterials based on isogeometric analysis. *Comput Methods Appl Mech Eng*. 2019;352:211-236.
23. Hassani B, Hinton E. A review of homogenization and topology optimization I—homogenization theory for media with periodic structure. *Comput Struct*. 1998;69(6):707-717.
24. Hassani B, Hinton E. A review of homogenization and topology optimization II—analytical and numerical solution of homogenization equations. *Comput Struct*. 1998;69(6):719-738.
25. Sigmund O. Materials with prescribed constitutive parameters: an inverse homogenization problem. *Int J Solids Struct*. 1994;31(17):2313-2329.
26. Sigmund O. Tailoring materials with prescribed elastic properties. *Mech Mater*. 1995;20(4):351-368.

27. Hassani B, Hinton E. A review of homogenization and topology optimization III—topology optimization using optimality criteria. *Comput Struct*. 1998;69(6):739-756.
28. Liu J, Gaynor AT, Chen S, et al. Current and future trends in topology optimization for additive manufacturing. *Struct Multidiscip Optim*. 2018;57(6):2457-2483.
29. Zegard T, Paulino GH. Bridging topology optimization and additive manufacturing. *Struct Multidiscip Optim*. 2016;53(1):175-192.
30. Fernandez F, Compel WS, Lewicki JP, Tortorelli DA. Optimal design of fiber reinforced composite structures and their direct ink write fabrication. *Comput Methods Appl Mech Eng*. 2019;353:277-307.
31. Gibson LJ, Ashby MF. *Cellular Solids: Structure and Properties*. Cambridge, MA: Cambridge University Press; 1999.
32. Pasini D, Guest JK. Imperfect architected materials: mechanics and topology optimization. *MRS Bull*. 2019;44(10):766-772.
33. Zhang XS, de Sturler E, Paulino GH. Stochastic sampling for deterministic structural topology optimization with many load cases: density-based and ground structure approaches. *Comput Methods Appl Mech Eng*. 2017;325:463-487.
34. Tsay J, Arora J. Optimum design of nonlinear structures with path dependent response. *Struct Optim*. 1989;1(4):203-213.
35. Vidal C, Lee H-S, Haber R. The consistent tangent operator for design sensitivity analysis of history-dependent response. *Comput Syst Eng*. 1991;2(5–6):509-523.
36. Michaleris P, Tortorelli DA, Vidal CA. Tangent operators and design sensitivity formulations for transient non-linear coupled problems with applications to elastoplasticity. *Int J Numer Methods Eng*. 1994;37(14):2471-2499.
37. Behrou R, Lawry M, Maute K. Level set topology optimization of structural problems with interface cohesion. *Int J Numer Methods Eng*. 2017;112(8):990-1016.
38. Alberdi R, Zhang G, Li L, Khandelwal K. A unified framework for nonlinear path-dependent sensitivity analysis in topology optimization. *Int J Numer Methods Eng*. 2018;115(1):1-56.
39. Swan CC, Kosaka I. Voigt–Reuss topology optimization for structures with nonlinear material behaviors. *Int J Numer Methods Eng*. 1997;40(20):3785-3814.
40. James KA, Waisman H. Topology optimization of viscoelastic structures using a time-dependent adjoint method. *Comput Methods Appl Mech Eng*. 2015;285:166-187.
41. Bendsøe MP, Díaz AR. A method for treating damage related criteria in optimal topology design of continuum structures. *Struct Optim*. 1998;16(2–3):108-115.
42. James KA, Waisman H. Failure mitigation in optimal topology design using a coupled nonlinear continuum damage model. *Comput Methods Appl Mech Eng*. 2014;268:614-631.
43. Yi B, Zhou Y, Yoon GH, Saitou K. Topology optimization of functionally-graded lattice structures with buckling constraints. *Comput Methods Appl Mech Eng*. 2019;354:593-619.
44. Abueidda DW, Koric S, Sobh NA. Topology optimization of 2D structures with nonlinearities using deep learning. *Comput Struct*. 2020;237:106283.
45. Gea HC, Luo J. Topology optimization of structures with geometrical nonlinearities. *Comput Struct*. 2001;79(20–21):1977-1985.
46. Wang F, Lazarov BS, Sigmund O, Jensen JS. Interpolation scheme for fictitious domain techniques and topology optimization of finite strain elastic problems. *Comput Methods Appl Mech Eng*. 2014;276:453-472.
47. Chi H, Ramos DL, Ramos AS Jr, Paulino GH. On structural topology optimization considering material nonlinearity: plane strain versus plane stress solutions. *Adv Eng Softw*. 2019;131:217-231.
48. Zhang G, Khandelwal K. Computational design of finite strain auxetic metamaterials via topology optimization and nonlinear homogenization. *Comput Methods Appl Mech Eng*. 2019;356:490-527.
49. Bruns TE, Tortorelli DA. Topology optimization of non-linear elastic structures and compliant mechanisms. *Comput Methods Appl Mech Eng*. 2001;190(26-27):3443-3459.
50. Wallin M, Ivarsson N, Tortorelli D. Stiffness optimization of non-linear elastic structures. *Comput Methods Appl Mech Eng*. 2018;330:292-307.
51. Wallin M, Jönsson V, Wingren E. Topology optimization based on finite strain plasticity. *Struct Multidiscip Optim*. 2016;54(4):783-793.
52. Li L, Zhang G, Khandelwal K. Design of energy dissipating elastoplastic structures under cyclic loads using topology optimization. *Struct Multidiscip Optim*. 2017;56(2):391-412.
53. Zhao T, Ramos AS Jr, Paulino GH. Material nonlinear topology optimization considering the von Mises criterion through an asymptotic approach: max strain energy and max load factor formulations. *Int J Numer Methods Eng*. 2019;118(13):804-828.
54. Schwarz S, Maute K, Ramm E. Topology and shape optimization for elastoplastic structural response. *Comput Methods Appl Mech Eng*. 2001;190(15):2135-2155.
55. Li L, Zhang G, Khandelwal K. Topology optimization of energy absorbing structures with maximum damage constraint. *Int J Numer Methods Eng*. 2017;112(7):737-775.
56. Maute K, Schwarz S, Ramm E. Adaptive topology optimization of elastoplastic structures. *Struct Optim*. 1998;15(2):81-91.
57. Nakshatrala P, Tortorelli D. Topology optimization for effective energy propagation in rate-independent elastoplastic material systems. *Comput Methods Appl Mech Eng*. 2015;295:305-326.
58. Zhang G, Li L, Khandelwal K. Topology optimization of structures with anisotropic plastic materials using enhanced assumed strain elements. *Struct Multidiscip Optim*. 2017;55(6):1965-1988.
59. Alberdi R, Khandelwal K. Topology optimization of pressure dependent elastoplastic energy absorbing structures with material damage constraints. *Finite Elem Anal Des*. 2017;133:42-61.

60. Kato J, Hoshiba H, Takase S, Terada K, Kyoya T. Analytical sensitivity in topology optimization for elastoplastic composites. *Struct Multidiscip Optim*. 2015;52(3):507-526.
61. Ivarsson N, Wallin M, Tortorelli D. Topology optimization of finite strain viscoplastic systems under transient loads. *Int J Numer Methods Eng*. 2018;114(13):1351-1367.
62. Ivarsson N, Wallin M, Tortorelli DA. Topology optimization for designing periodic microstructures based on finite strain viscoplasticity. *Struct Multidiscip Optim*. 2020;61(6):2501-2521.
63. Kennedy GJ, Chin TW. A sequential convex optimization method for multimaterial compliance design problems. *Comput Struct*. 2019;212:110-124.
64. Pizzolato A, Sharma A, Maute K, Sciacovelli A, Verda V. Multi-scale topology optimization of multi-material structures with controllable geometric complexity—applications to heat transfer problems. *Comput Methods Appl Mech Eng*. 2019;357:112552.
65. Sanders ED, Aguiló MA, Paulino GH. Multi-material continuum topology optimization with arbitrary volume and mass constraints. *Comput Methods Appl Mech Eng*. 2018;340:798-823.
66. Zhang XS, Paulino GH, Ramos AS. Multi-material topology optimization with multiple volume constraints: a general approach applied to ground structures with material nonlinearity. *Struct Multidiscip Optim*. 2018;57(1):161-182.
67. Alberdi R, Khandelwal K. Bi-material topology optimization for energy dissipation with inertia and material rate effects under finite deformations. *Finite Elem Anal Des*. 2019;164:18-41.
68. Swan C, Kosaka I. Homogenization-based analysis and design of composites. *Comput Struct*. 1997;64(1–4):603-621.
69. Swan C, Arora JS. Topology design of material layout in structured composites of high stiffness and strength. *Struct Optim*. 1997;13(1):45-59.
70. Wang F, Sigmund O, Jensen JS. Design of materials with prescribed nonlinear properties. *J Mech Phys Solids*. 2014;69:156-174.
71. Chen W, Xia L, Yang J, Huang X. Optimal microstructures of elastoplastic cellular materials under various macroscopic strains. *Mech Mater*. 2018;118:120-132.
72. Alberdi R, Khandelwal K. Design of periodic elastoplastic energy dissipating microstructures. *Struct Multidiscip Optim*. 2019;59(2):461-483.
73. Carstensen JV, Lotfi R, Guest JK, Chen W, Schroers J. Topology optimization of cellular materials with maximized energy absorption. Proceedings of the ASME 2015 International Design Engineering Technical Conferences and Computers and Information in Engineering Conference. Volume 2B: 41st Design Automation Conference. Boston, MA. August 2-5, 2015:V02BT03A014.
74. Bazant Zdenek, P. *Scaling of Structural Strength (Second Edition)*. Oxford, UK: Butterworth-Heinemann; 2005.
75. Bischoff PH, Perry SH. Compressive behaviour of concrete at high strain rates. *Mater Struct*. 1991;24(6):425-450.
76. Bauer J, Hengsbach S, Tesari I, Schwaiger R, Kraft O. High-strength cellular ceramic composites with 3D microarchitecture. *Proc Natl Acad Sci*. 2014;111(7):2453-2458.
77. Amir O, Bogomolny M. Topology optimization for conceptual design of reinforced concrete structures. Paper presented at: 9th World Congress on Structural and Multidisciplinary Optimization; 2011.
78. Amir O. A topology optimization procedure for reinforced concrete structures. *Comput Struct*. 2013;114:46-58.
79. Amir O, Sigmund O. Reinforcement layout design for concrete structures based on continuum damage and truss topology optimization. *Struct Multidiscip Optim*. 2013;47(2):157-174.
80. Zhou M, Rozvany G. The COC algorithm, part II: topological, geometrical and generalized shape optimization. *Comput Methods Appl Mech Eng*. 1991;89(1–3):309-336.
81. Bendsøe MP. Optimal shape design as a material distribution problem. *Struct Optim*. 1989;1(4):193-202.
82. Anthoine A. Derivation of the in-plane elastic characteristics of masonry through homogenization theory. *Int J Solids Struct*. 1995;32(2):137-163.
83. Michel J-C, Moulinec H, Suquet P. Effective properties of composite materials with periodic microstructure: a computational approach. *Comput Methods Appl Mech Eng*. 1999;172(1–4):109-143.
84. Miehe C, Koch A. Computational micro-to-macro transitions of discretized microstructures undergoing small strains. *Arch Appl Mech*. 2002;72(4–5):300-317.
85. Zienkiewicz OC, Taylor RL, Zhu JZ. *The Finite Element Method: Its Basis and Fundamentals (Seventh Edition)*. Oxford, UK: Butterworth-Heinemann; 2013.
86. Bonet J, Wood RD. *Nonlinear Continuum Mechanics for Finite Element Analysis*. Cambridge, MA: Cambridge University Press; 1997.
87. Simo JC, Hughes TJ. *Computational Inelasticity*. Berlin, Germany: Springer Science & Business Media; 2006.
88. Wilkins M. Calculation of elastic-plastic flow. In: Alder B, Perribach S, Eotenberg M, et al., eds. *Methods of Computational Physics*. New York, NY: Academic Press; 1964.
89. Allaire G, Jouve F, Toader A-M. Structural optimization using sensitivity analysis and a level-set method. *J Comput Phys*. 2004;194(1):363-393.
90. Wang MY, Wang X, Guo D. A level set method for structural topology optimization. *Comput Methods Appl Mech Eng*. 2003;192(1–2):227-246.
91. Jog CS, Haber RB. Stability of finite element models for distributed-parameter optimization and topology design. *Comput Methods Appl Mech Eng*. 1996;130(3–4):203-226.
92. Sigmund O, Petersson J. Numerical instabilities in topology optimization: a survey on procedures dealing with checkerboards, mesh-dependencies and local minima. *Struct Optim*. 1998;16(1):68-75.
93. Jansson S. Homogenized nonlinear constitutive properties and local stress concentrations for composites with periodic internal structure. *Int J Solids Struct*. 1992;29(17):2181-2200.

94. Sobieszczanski-Sobieski J. Sensitivity of complex, internally coupled systems. *AIAA J*. 1990;28(1):153-160.
95. Sethian JA, Wiegmann A. Structural boundary design via level set and immersed interface methods. *J Comput Phys*. 2000;163(2):489-528.
96. Almeida SR, Paulino GH, Silva EC. Layout and material gradation in topology optimization of functionally graded structures: a global–local approach. *Struct Multidiscip Optim*. 2010;42(6):855-868.
97. Wang Y, Luo Z, Zhang N, Kang Z. Topological shape optimization of microstructural metamaterials using a level set method. *Comput Mater Sci*. 2014;87:178-186.
98. Svanberg K. The method of moving asymptotes—a new method for structural optimization. *Int J Numer Methods Eng*. 1987;24(2):359-373.

**How to cite this article:** Abueidda DW, Kang Z, Koric S, James KA, Jasiuk IM. Topology optimization for three-dimensional elastoplastic architected materials using a path-dependent adjoint method. *Int J Numer Methods Eng*. 2021;1–22. https://doi.org/10.1002/nme.6604